JEM Journal of Experimental Medicine

ARTICLE

Xbp1 controls the reparative function of intestinal ILC2s during colitis

Yanyan Cui[1*], Zixiao Zhao[2*], Jing Shen[1*], Yatai Chen[1*], Qiuheng Tian[1*], Yang Liu[1], Yunjiao Zhai[1], Bowen Xu[3], Jiajie Hou[4,5], Chunyang Li[6], Yanbo Yu[1,7], Xiaohuan Guo[8,9], Ju Qiu[10], Detian Yuan[3], and Shiyang Li[1,7,11]

Ulcerative colitis (UC) is primarily characterized by inflammation-induced tissue damage, but impaired tissue repair also drives disease progression. This study demonstrates group 2 innate lymphoid cells (ILC2s), key players in tissue repair, are dysfunctional in UC and experimental colitis due to disrupted endoplasmic reticulum protein processing. We show that the pro-repair function of gut ILC2s depends on the IRE1α-Xbp1 branch of unfolded protein response (UPR), supported by IL-25 and suppressed by interferon-γ (IFN-γ). During colitis, loss of IL-25 and rise of IFN-γ hinder *Xbp1* mRNA splicing, weakening ILC2s' ability to mediate tissue repair. Mechanistically, spliced Xbp1 drives folate-dependent one-carbon (1C) metabolism by promoting dihydrofolate reductase expression. Translationally, the 1C metabolite adenosine 5′-monophosphate alleviated colitis in both ILC2-specific *Xbp1* knockout and wild-type mice. Our findings highlight the UPR's role in sensing gut environment to regulate ILC2 function and suggest folate-mediated 1C metabolism as a potential target for UC therapy.

Introduction

Ulcerative colitis (UC) is a chronic inflammatory disorder affecting the lining of the large intestine (Sharma et al., 2022). Aberrant inflammation in UC leads to tissue damage. Current therapies primarily target inflammation, such as monoclonal antibodies against TNF or IL-23 (Moschen et al., 2019; Neurath, 2024). However, impaired tissue repair also contributes to UC progression. Tissue repair involves various gut cell compartments, with group 2 innate lymphoid cells (ILC2s) playing a pivotal role (Yin et al., 2022; Zaiss et al., 2015). Despite this, the dynamics and regulatory mechanisms of ILC2s in UC remain unclear.

The pro-repair function of ILC2s is mediated by type 2 cytokines, predominantly the pro-healing molecule amphiregulin (Areg), along with IL-5 and IL-13 (Vivier et al., 2018; Zaiss et al., 2015). These effector molecules aid in gut tissue repair by facilitating stem cell turnover, activating tuft cells, and/or augmenting goblet cell mucin production (von Moltke et al., 2016). The activity of ILC2s is fine-tuned by various tissue signals, including prostaglandins, neuropeptides, and cytokines such as IL-25, IL-33, thymic stromal lymphopoietin (TSLP), and IL-18 (Kato, 2019). In UC, the inflamed gut undergoes significant changes, including dysregulation of the unfolded protein response (UPR) in the gut epithelium, which contributes to the pathogenesis of colitis (Kaser et al., 2008). Notably, most studies on UPR in colitis focus on intestinal epithelial cells (Kaser and Blumberg, 2009; Kaser et al., 2008). It remains unclear whether UPR signaling affects the intestinal immune compartment, particularly gut ILC2s, and contributes to UC progression.

In eukaryotic cells, instances of protein misfolding are commonplace, prompting eukaryotic cells to evolve the UPR to alleviate the burden of unfolded or misfolded proteins and ensure protein folding fidelity (Hetz et al., 2020). The UPR signaling pathways in mammalian cells consist of three primary cascades initiated by endoplasmic reticulum (ER) transmembrane protein sensors, including inositol-requiring enzyme 1α and 1β (IRE1α/1β), protein kinase RNA-like ER kinase (PERK), and activating transcription factor 6 (ATF6), and these pathways are orchestrated to safeguard cells from excessive ER stress (Grootjans et al., 2016). Beyond the gastrointestinal tract, the UPR is a critical regulator in various immune cell types. In lymphocytes,

[1]Department of Gastroenterology, Qilu Hospital of Shandong University, Advanced Medical Research Institute, Shandong University, Jinan, China; [2]Department of Digestive Endoscopy, The First Affiliated Hospital of Shandong First Medical University (Shandong Provincial Qianfoshan Hospital), Jinan, China; [3]Department of Biochemistry and Molecular Biology, School of Basic Medical Sciences, Shandong University, Jinan, China; [4]Faculty of Health Sciences, Cancer Centre, University of Macau, Macau, China; [5]MOE Frontier Science Centre for Precision Oncology, University of Macau, Macau, China; [6]Key Laboratory for Experimental Teratology of Ministry of Education and Department of Histology and Embryology, School of Basic Medical Sciences, Cheeloo College of Medicine, Shandong University, Jinan, China; [7]Shandong Provincial Clinical Research Center for Digestive Diseases, Jinan, China; [8]Institute for Immunology, School of Medicine, Tsinghua University, Beijing, China; [9]Beijing Key Lab for Immunological Research on Chronic Diseases, Tsinghua University, Beijing, China; [10]CAS Key Laboratory of Tissue Microenvironment and Tumor, Shanghai Institute of Nutrition and Health, University of Chinese Academy of Sciences, Chinese Academy of Sciences, Shanghai, China; [11]Key Laboratory for Experimental Teratology of Ministry of Education, Shandong University, Jinan, China.

*Y. Cui, Z. Zhao, J. Shen, Y. Chen, and Q. Tian contributed equally to this paper. Correspondence to Shiyang Li: lishiyang@sdu.edu.cn.

Xbp1 plays a significant role in the differentiation and function of $CD8^+$ and $CD4^+$ T cells, as well as B cells during infections, allergic responses, and cancer (Di Conza et al., 2023; Dong et al., 2019; Kamimura and Bevan, 2008; Song et al., 2018; Zeng et al., 2022). Additionally, UPR signaling affects myeloid cells, including dendritic cells, macrophages, and Kupffer cells across different organs and diseases (Iwakoshi et al., 2007; Martinon et al., 2010; Rao et al., 2014).

In this study, we observed reduced cell numbers and effector molecule production in large intestinal ILC2/3 compartments in patients with UC and experimental colitis mice. Single-cell RNA sequencing (scRNA-seq) showed significant disruption in the ER protein processing pathway in inflamed gut ILC2s. Our screening of UPR pathways identified the IRE1α-Xbp1 branch as crucial for maintaining gut ILC2s, while PERK and ATF6 are less involved. Accordingly, colonic ILC2s from patients with UC had lower spliced Xbp1 (XBP1s) protein levels compared with healthy controls, and this reduction correlated with more severe colitis, as reflected by higher Ulcerative Colitis Endoscopic Index of Severity (UCEIS) scores. Mechanistically, IL-25 activated p38 signaling, promoting IRE1α phosphorylation and *Xbp1* mRNA splicing, and this axis was suppressed by colitis-elevated interferon-γ (IFN-γ). In addition, Xbp1s, as a transcription factor, bound to the locus and sustains the transcription of *Dhfr*, which encodes an essential enzyme of folate-mediated one-carbon (1C) metabolism. Among the key metabolites of 1C metabolism, only adenosine 5′-monophosphate (AMP) maintained intestinal ILC2 function by supporting cyclic AMP (cAMP) generation. Translationally, AMP supplementation ameliorated experimental colitis in wild-type (WT) mice and those with ILC2-specific *Xbp1* deletion. These findings illuminate the underappreciated role of Xbp1 in sensing the gut milieu to direct metabolic homeostasis and tissue repair function of gut ILC2s, highlighting folate-mediated 1C metabolism in ILC2s as a potential immunometabolic target for UC therapy.

Results

Impaired colonic ILC2s linked to disrupted IRE1α-Xbp1 branch of UPR in UC and experimental colitis

To explore alterations in the tissue repair–associated ILC compartment in UC, we conducted an analysis using publicly available scRNA-seq data (GSE125527) (Boland et al., 2020). Our investigation unveiled a significant decline in the subcluster of ILC2/3 within the colons of patients with UC (Fig. 1 A; Fig. S1, A and B; and Table S1). It is worth noting that scRNA-seq analysis identifies ILC2s and ILC3s as a mixed population in the human colon, although distinct in mice (Mennillo et al., 2024). Further analysis indicated a notable reduction in the mRNA levels of *AREG*, a pivotal pro-healing effector molecule of ILC2s, in the ILC2/3 compartment of the UC colon (Fig. 1 B). Of note, the signature genes associated with ILC3s, a pivotal subset known for their contribution to tissue repair via IL-22 secretion, exhibited upregulation within the ILC2/3 population (Fig. 1 B). However, *IL22* itself was not detected in this dataset (Fig. 1 B).

We next conducted transcriptomic analysis on colonic ILC2/3 compartment of patients with UC or healthy donors (Fig. 1 C). Kyoto Encyclopedia of Genes and Genomes (KEGG) enrichment analysis of the differentially expressed genes (DEGs) between UC and healthy controls revealed that the protein processing in ER was one of the main enriched pathways altered in the population of ILC2/3 of patients with UC (Fig. 1 C). The protein processing pathway in ER is intricately regulated by the UPR, which orchestrates three downstream pathways, namely, IRE1α-Xbp1, PERK-eIF2α, and ATF6, all critical for maintaining proper protein folding (Grootjans et al., 2016). However, among the enriched genes contained in the protein processing in the ER pathway, only the expression of *ERN1* (encoding IRE1α) was significantly decreased in the ILC2/3 population of patients with UC (Fig. 1 D and Fig. S1 C). ER stress activates IRE1α via the UPR, which triggers phosphorylation of IRE1α and activates its endonuclease function (Han et al., 2009). As an endonuclease, IRE1α cleaves a specific 26-nucleotide intron from *Xbp1* mRNA. This splicing event causes a frameshift during translation, generating the spliced form of Xbp1, Xbp1s. The Xbp1s acts as an active transcription factor, driving the adaptive cellular response to stress. Specifically, XBP1s protein levels in colonic ILC2s were lower in patients with UC compared with healthy donors (Fig. 1 E and Table S2). Moreover, reduced XBP1s levels in colonic ILC2s were associated with more severe colitis, as evidenced by higher UCEIS scores in patients with UC (Fig. 1 F). In contrast, XBP1s expression in colonic ILC3s did not differ significantly between healthy donors and patients with UC (Fig. 1 G), and the correlation between XBP1s protein levels in ILC3s and UCEIS was markedly weaker compared with that in ILC2s (Fig. 1 H). Of note, XBP1s protein levels in colonic ILC2s are higher than those in ILC3s in healthy individuals (Fig. S1 D). To investigate the essential role of XBP1s in the production of pro-healing molecule, AREG, in human ILC2s, lamina propria mononuclear cells (LPMNCs) from healthy donors were isolated and treated with toyocamycin, a well-recognized inhibitor of *Xbp1* mRNA splicing (Ri et al., 2012). This intervention led to a notable decrease in AREG expression within human colonic ILC2s (Fig. 1, I and J; and Fig. S1 E).

To corroborate these findings, we induced colitis in mice using dextran sulfate sodium (DSS), a well-established model for mimicking human UC, and confirmed a substantial decrease in large intestinal ILC2s through scRNA-seq analysis (Fig. 1 K; Fig. S1, F and G; and Table S3). Subsequent analysis unveiled a notable decrease in type 2 cytokines, including *Areg*, *Il5*, and *Il13*, in gut ILC2s following DSS administration (Fig. S1, H and I). Notably, scRNA-seq analysis of mouse colon delineated ILC3s as a distinct subset, showing a decline during DSS-induced colitis (Fig. 1 K). Despite the reduction in ILC3s, the mRNA levels of *Il22*, encoding a key cytokine crucial for tissue repair, were elevated in ILC3s in the context of colitis (Fig. S1 J). Accordingly, the protein processing in ER pathway was also prominently enriched in the KEGG enrichment analysis of colonic ILC2s from mice with DSS-induced colitis (Fig. S1 K). Of note, RNA levels of the IL-2 receptor subunits (*Il2ra*, *Il2rb*, *Il2rg*) were downregulated in colonic ILC2s during DSS-induced colitis (Fig. S1 L).

Flow cytometry analysis of lamina propria lymphocytes (LPLs) from DSS-treated mice supported the reduction in large intestinal ILC2s and compromised production of effector

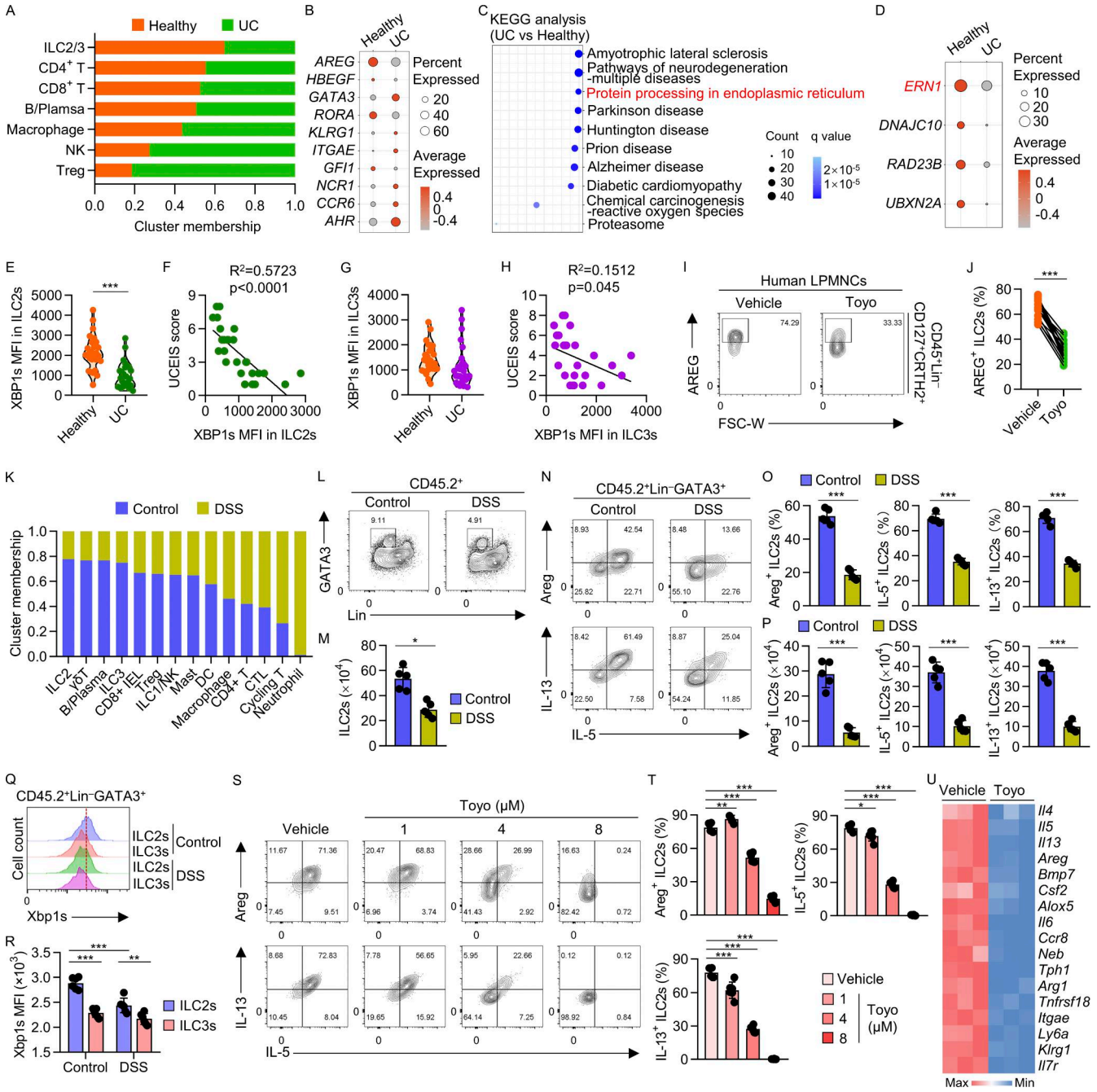

Figure 1. **Compromised colonic ILC2s in colitis and IRE1α-mediated branch of UPR sustain the function of gut ILC2s. (A)** Proportions of indicated immune cell compartments by conducting scRNA-seq analysis with CD45⁺ immune cells isolated from the colonic biopsies of patients with UC or healthy donors (GSE125527). **(B)** Dot plot showed the levels of ILC2 or ILC3 signature genes in ILC2/3 population. **(C)** KEGG pathway enrichment analysis of DEGs in ILC2/3 cluster between healthy donors and patients with UC. **(D)** Dot plot showed the downregulation of genes involved in the protein processing in ER pathways in ILC2/3 cells of patients with UC in Fig. 1 C. **(E and F)** Flow cytometry analysis of the MFI of XBP1s in colonic ILC2s (CD45⁺Lin⁻CD127⁺CRTH2⁺) of healthy donors or patients with UC (n = 27 per group) (E). Correlation analysis between XBP1s MFI in ILC2s and UCEIS score (F). **(G and H)** Flow cytometry analysis of the MFI of XBP1s in colonic ILC3s (CD45⁺Lin⁻CD127⁺CRTH2⁻CD117⁺) of healthy donors or patients with UC (n = 27 per group) (G). Correlation analysis between XBP1s MFI in ILC3s and UCEIS score (H). **(I and J)** Human colonic LPMNCs were treated with toyocamycin (Toyo) at 25 μM for 16 h. Flow cytometry analysis of AREG expression in ILC2s after gating on CD45⁺Lin⁻CD127⁺CRTH2⁺ (I). Percentage of AREG⁺ ILC2s out of total ILC2s (CD45⁺Lin⁻CD127⁺CRTH2⁺) (J). Connected lines are samples from the same clinical samples (n = 17). P value was determined by two-tailed paired Student's t test. **(K)** Mid-colon tissues were harvested from mice treated with 3% DSS for 6 days and subjected to scRNA-seq analysis. The scRNA-seq data served as the control group were generated from untreated mice by our team (GSE210415). CD45⁺ immune cells were extracted to analyze the proportions of indicated immune cell compartments. **(L–P)** WT mice were administered 3% DSS in drinking water for 6 days to induce colitis, followed by flow cytometry analysis of GATA3 expression after gating on CD45.2⁺Lin⁻ cells in large intestinal LPLs (L), absolute numbers of ILC2s (CD45.2⁺Lin⁻GATA3⁺) (M). Flow cytometry analysis of Areg, IL-5, and IL-13 expression in ILC2s (N), percentages (O) and absolute numbers (P) of Areg⁺, IL-5⁺, and IL-13⁺ ILC2s. Data were compiled from two independent experiments. Data are shown as the mean ± SD (n = 5 per group). **(Q and R)** Xbp1s expression in ILC2s (CD45.2⁺Lin⁻GATA3⁺) or ILC3s (CD45.2⁺Lin⁻RORγt⁺) from large intestinal LPLs of DSS-

treated or control mice detected by flow cytometry (Q). MFI of Xbp1s in ILC2s or ILC3s (R). Data were compiled from two independent experiments. Data are shown as the mean ± SD (n = 6 per group). **(S and T)** Sorted ILC2s ($Lin^-CD127^+KLRG1^+$) were cultured for 5 days in the presence of IL-2, IL-7, IL-25, and IL-33 (10 ng/ml each), and then treated with Toyo at the indicated concentrations for 16 h. Flow cytometry analyses of Areg, IL-5, and IL-13 expression in ILC2s ($CD45.2^+Lin^-GATA3^+$) (S). Percentages of $Areg^+$, $IL\text{-}5^+$, and $IL\text{-}13^+$ cells in ILC2s (T). Data were compiled from two independent experiments. Data are shown as the mean ± SD (n = 6 per group). **(U)** Heatmap of ILC2-characteristic genes by performing RNA-seq analysis with Toyo (4 µM) treated for 16 h or vehicle ILC2s. *P < 0.05, **P < 0.01, ***P < 0.001. MFI, mean fluorescence intensity.

molecules, particularly Areg, IL-5, and IL-13 by ILC2s (Fig. 1, L–P; and Fig. S1, M–R). This reduction was accompanied by decreased *Xbp1* mRNA splicing, as assessed by qRT-PCR using primers specific to total *Xbp1* (*Xbp1t*) and *Xbp1s* (Wei et al., 2021; Yang et al., 2022), as well as lower Xbp1s protein levels in colonic ILC2s from DSS-fed mice compared with controls (Fig. 1, Q and R; and Fig. S1 S). In contrast, no significant difference in Xbp1s protein levels was observed in colonic ILC3s between DSS-induced colitis mice and controls (Fig. 1, Q and R). Notably, Xbp1s protein levels in colonic ILC2s were higher than in ILC3s, both in control and in DSS-treated mice (Fig. 1, Q and R). Given the critical role of ILC2s in gut tissue repair, our study aimed to elucidate the mechanisms underlying the inhibition of ILC2s in the colon during colitis, focusing on the disrupted IRE1α-Xbp1 pathway and its impact on colonic ILC2s.

IRE1α-mediated branch of UPR sustains the function of gut ILC2s

To investigate the potential involvement of protein processing–associated signals in regulating colonic ILC2 homeostasis, sorted ILC2s from mice were treated with inhibitors targeting three UPR pathways, including IRE1α-Xbp1, PERK-eIF2α, and ATF6, respectively. Subsequent flow cytometry analysis demonstrated that only IRE1α-Xbp1 inhibitor, toyocamycin, downregulated the production of effector molecules in ILC2s, rather than PERK or ATF6 inhibitors (Fig. 1, S and T; and Fig. S2, A–F). This observation was further reinforced by RNA-seq analysis revealing a marked decrease in the expression of ILC2 signature genes in toyocamycin-treated ILC2s (Fig. 1 U). In accordance, intraperitoneal injection of toyocamycin into WT mice also suppressed the production of Areg, IL-5, and IL-13 in ILC2s *in vivo* (Fig. S2, G–J). The inhibitory effect of toyocamycin on gut ILC2s implies the necessity of Xbp1s, the transcriptionally active spliced form of Xbp1, for the production of effector molecules in these cells. Taken together, these findings suggest that gut inflammation results in diminished *Xbp1* mRNA splicing in colonic ILC2s, contributing to the reduced production of effector molecules by these cells.

Xbp1s regulates colonic ILC2s intrinsically and is essential for restraining colitis progression

Since ILC2s are the main source of IL-5 in the gut (Fig. S2 K), $Il5^{RFP\text{-}Cre}$ mice have been applied for the deletion of genes in ILC2s (Nussbaum et al., 2013). Thus, to ascertain the cell-intrinsic role of Xbp1 in colonic ILC2s, we generated mice with ILC2-specific deletion of *Xbp1* by crossing $Xbp1^{f/f}$ mice with $Il5^{RFP\text{-}Cre}$ mice, resulting in $Xbp1^{f/f}Il5^{RFP\text{-}Cre}$ mice. Under the steady state, $Xbp1^{f/f}Il5^{RFP\text{-}Cre}$ mice exhibited reduced numbers of colonic ILC2s and impaired production of Areg, IL-5, and IL-13 compared with $Xbp1^{+/+}Il5^{RFP\text{-}Cre}$ control mice (Fig. S2, L–P). Notably, cell death of *ex vivo* ILC2s from $Xbp1^{f/f}Il5^{RFP\text{-}Cre}$ mice was comparable to that in $Xbp1^{+/+}Il5^{RFP\text{-}Cre}$ mice at steady state (Fig. S2 Q). However, *in vitro*–expanded *Xbp1*-deleted ILC2s showed significantly higher cell death compared with *Xbp1*-intact ILC2s (Fig. S2 Q). This difference may stem from compensation by residual ILC2s without *Xbp1* deletion in $Xbp1^{f/f}Il5^{RFP\text{-}Cre}$ mice. Furthermore, *in vitro*–cultured ILC2s from $Xbp1^{f/f}Il5^{RFP\text{-}Cre}$ mice exhibited dramatic reduction in the cell numbers and decreased production of Areg, IL-5, and IL-13, compared with ILC2s from $Xbp1^{+/+}Il5^{RFP\text{-}Cre}$ mice (Fig. 2, A–C; and Fig. S2 R). This reduction was restored by retroviral expression of Xbp1s in *Xbp1*-deleted ILC2s (Fig. 2, A–C; and Fig. S2, R–U), demonstrating the critical role of *Xbp1* mRNA splicing in maintaining gut ILC2s.

In addition, we performed an *in vivo* competitive transfer experiment. Large intestinal ILC2s from $Xbp1^{+/+}Il5^{RFP\text{-}Cre}$ (CD45.1/CD45.1) and $Xbp1^{f/f}Il5^{RFP\text{-}Cre}$ (CD45.2/CD45.2) were transferred at a 1:1 ratio into $Rag2^{-/-}Il2rg^{-/-}$ mice (Fig. S2 V), which are deficient in T, B cells, and ILCs (Abt et al., 2015; Spolski et al., 2018). Two wk after transfer, LPLs were isolated from the large intestine, and ILC2s were distinguished based on congenic markers to trace their source (Fig. 2 D). A marked decrease in the number of *Xbp1*-deficient ILC2s was observed in the large intestine (Fig. 2, E and F). In addition, ILC2s from $Xbp1^{f/f}Il5^{RFP\text{-}Cre}$ mice showed reduced expression of Areg, IL-5, and IL-13 compared with those from $Xbp1^{+/+}Il5^{RFP\text{-}Cre}$ mice (Fig. 2, E and F).

To explore how Xbp1 deficiency in gut ILC2s affects colitis progression, $Xbp1^{f/f}Il5^{RFP\text{-}cre}$ mice were subjected to DSS-induced colitis. $Xbp1^{f/f}Il5^{RFP\text{-}cre}$ mice showed aggravated DSS-induced colitis as revealed by higher disease activity index (DAI), shortened colon length, and more severe histopathological damage (Fig. 2, G–L). Moreover, the numbers of ILC2s and the expression of Areg, IL-5, and IL-13 in large intestinal ILC2s were decreased in $Xbp1^{f/f}Il5^{RFP\text{-}cre}$ mice compared with those in $Xbp1^{+/+}Il5^{RFP\text{-}cre}$ control mice following DSS treatment (Fig. 2, M–Q). While ILC2s are also a source of IL-9, which contributes to UC pathogenesis (Gerlach et al., 2014; Nalleweg et al., 2015; Shohan et al., 2018; Turner et al., 2013; Wilhelm et al., 2011), quantitative RT-PCR (qRT-PCR) analysis revealed that *Il9* expression was significantly lower in ILC2s from $Xbp1^{f/f}Il5^{RFP\text{-}cre}$ mice than those from $Xbp1^{+/+}Il5^{RFP\text{-}cre}$ control mice (Fig. S2 W). Moreover, *Il9* expression was also reduced in ILC2s from DSS-treated colitis mice compared with controls (Fig. S2 X), suggesting that ILC2-derived IL-9 does not contribute to the exacerbation of colitis.

Prior research shows that ILC3-specific deletion of *Ire1α*, the upstream regulator of *Xbp1* splicing, worsens colitis (Cao et al., 2024). To evaluate ILC3-intrinsic Xbp1 in colitis, we generated $Xbp1^{f/f}$*Rorc-cre* mice with ILC3/T cell–specific *Xbp1* deletion. After DSS treatment, $Xbp1^{f/f}$*Rorc-cre* mice showed similar colitis

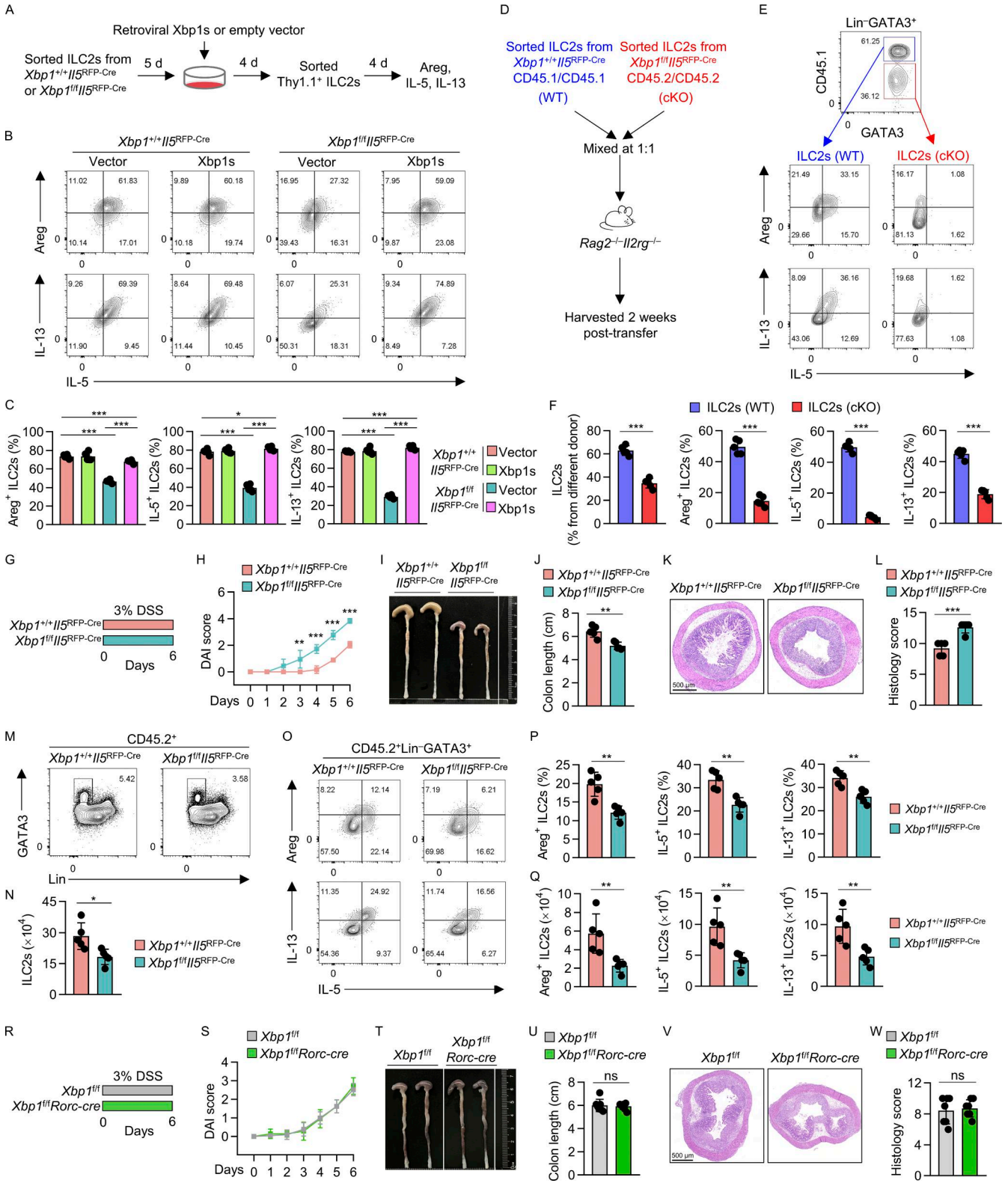

Figure 2. **Xbp1s regulates colonic ILC2s intrinsically and is essential for restraining colitis progression. (A–C)** Large intestinal ILC2s (Lin⁻CD127⁺KLRG1⁺) were sorted from *Xbp1*$^{f/f}$*Il5*$^{RFP\text{-}Cre}$ or littermate *Xbp1*$^{+/+}$*Il5*$^{RFP\text{-}Cre}$ mice and underwent retroviral transduction of Xbp1s with IRES-controlled Thy1.1 expression to label transduced cells. Thy1.1⁺ cells after gating on Lin⁻CD45.2⁺ were sorted and cultured for 4 days. Experimental design (A). Areg, IL-5, and IL-13 expression in ILC2s (CD45.2⁺Lin⁻GATA3⁺) was analyzed by flow cytometry (B). Percentages of Areg⁺, IL5⁺, and IL-13⁺ cells in ILC2s (C). Data were compiled from two independent experiments. Data are shown as the mean ± SD (n = 6 per group). **(D–F)** Sorted large intestinal ILC2s (Lin⁻CD127⁺KLRG1⁺) from WT (*Xbp1*$^{+/+}$*Il5*$^{RFP\text{-}Cre}$) (CD45.1/CD45.1) or cKO (*Xbp1*$^{f/f}$*Il5*$^{RFP\text{-}Cre}$) (CD45.2/CD45.2) age- and sex-matched mice were mixed equally (2 × 10⁵ cells in total) and transferred into *Rag2*$^{-/-}$*Il2rg*$^{-/-}$ littermate recipient mice. Experimental design (D). Flow cytometry analyses of CD45.1 and GATA3 expression (upper), Areg, IL-5, and IL-13

expression (bottom) after gating on indicated populations (E). Proportion of ILC2s (Lin⁻GATA3⁺) from different donor, and percentages of Areg⁺, IL-5⁺, and IL-13⁺ cells in recovered WT or cKO ILC2s (F). Data were compiled from two independent experiments. Data are shown as the mean ± SD (n = 5 per group). **(G–Q)** *Xbp1*$^{+/+}$*Il5*$^{RFP\text{-}Cre}$ and *Xbp1*$^{f/f}$*Il5*$^{RFP\text{-}Cre}$ mice were fed with 3% DSS in drinking water for 6 days to induce colitis model. Experimental design (G) and DAI scores (H) were monitored at the indicated time points. Representative large intestine images (I). Lengths of colons (J). Representative H&E staining of the colon. Scale bar, 500 µm (K). Histological severity scores (L). Flow cytometry analysis of GATA3 expression after gating on CD45.2⁺Lin⁻ cells in large intestinal LPLs (M), absolute numbers of ILC2s (CD45.2⁺Lin⁻GATA3⁺) (N). Flow cytometry analysis of Areg, IL-5, and IL-13 expression in ILC2s (O). Percentages (P) and absolute numbers (Q) of Areg⁺, IL-5⁺, and IL-13⁺ ILC2s. Data were compiled from two independent experiments. Data are shown as the mean ± SD (n = 5 per group). **(R–W)** *Xbp1*$^{f/f}$ and *Xbp1*$^{f/f}$*Rorc-cre* mice were fed with 3% DSS for 6 days to induce colitis model. Experimental design (R). DAI scores (S). Representative large intestine images (T). Lengths of colons (U). Representative H&E staining of the colon. Scale bar, 500 µm (V). Histological severity scores (W). Data were compiled from two independent experiments and are shown as the mean ± SD (n = 7 per group). *P < 0.05, **P < 0.01, ***P < 0.001.

severity to littermate controls, although a slight reduction of IL-22 production by ILC3s was observed (Fig. 2, R–W; and Fig. S2, Y and Z). Collectively, these findings underscore the intrinsic role of Xbp1 in governing gut ILC2s and highlight its crucial function in restraining colitis progression.

Colitis-associated milieu eliminates *Xbp1* mRNA splicing in colonic ILC2s

To elucidate the environmental factors regulating *Xbp1* mRNA splicing in gut ILC2s and sustaining their function, we analyzed the RNA levels of the known regulators of ILC2s, including *Il25*, *Il33*, and *Tslp*, and pro-inflammatory cytokines *Ifng*, *Il1b*, *Il6*, and *Tnf*, in colonic tissues from DSS-treated mice using RNA-seq analysis (GSE210405) (Zheng et al., 2024). The data revealed a significant decrease in *Il25* transcript levels in DSS-treated mice, while *Il33* expression was notably increased and *Tslp* kept unaltered (Fig. 3 A). Accordingly, IL-25 was found specifically to promote *Xbp1* mRNA splicing and elevate Xbp1s protein levels in ILC2s, in contrast to IL-33 and TSLP (Fig. 3, B–D; and Fig. S3, A and B). Consistent with this observation, we noted a substantial loss of tuft cells, the primary source of IL-25 in the gut, during colitis progression (Fig. S3, C–I and Table S4).

Moreover, removal of IL-25 from large intestinal ILC2s cultured in the presence of IL-25 led to a dramatic reduction in *Xbp1* mRNA splicing and Xbp1s protein levels, accompanied by a marked decrease in Areg, IL-5, and IL-13 expression in ILC2s (Fig. 3, E–H; and Fig. S3, J and K). Of note, IL-25 removal–caused downregulation of Xbp1s, Areg, IL-5, and IL-13 in ILC2s was restored by resumption of IL-25 administration (Fig. 3, I–L; and Fig. S3, L and M). Together, these data underscore the role of tuft cells in secreting IL-25 to enhance *Xbp1* mRNA splicing and activate intestinal ILC2s.

During colitis, the RNA levels of pro-inflammatory cytokines, *Ifng*, *Il1b*, *Il6*, and *Tnf* were elevated as revealed by RNA-seq or scRNA-seq with colonic tissues from DSS-treated mice compared with controls (Fig. 3 A and Fig. S4 A). However, only IFN-γ specifically inhibited *Xbp1* mRNA splicing and downregulated Xbp1s protein levels in ILC2s, accompanied by a marked decrease in Areg, IL-5, and IL-13 expression, in contrast to IL-1β, IL-6, and TNF-α (Fig. 3, M–O; and Fig. S4, B and C). Moreover, IFN-γ treatment weakened the IL-25–enhanced Xbp1s expression and effector molecule production in ILC2s (Fig. 3, P–R; and Fig. S4, D and E). These findings underscore that reduced IL-25 and excessive IFN-γ productions during colitis disrupt *Xbp1* mRNA splicing and impair gut ILC2 function.

Accordingly, we observed that IL-25 levels were decreased, while IFN-γ levels were elevated in colon tissues during colitis compared with controls (Fig. 3, S and T), reflecting a dysregulated cytokine environment. To further investigate the role of IL-25 and IFN-γ in regulating the Xbp1s pathway in ILC2s *in vivo* and their impact on colitis progression, we further assessed the effects of restoring IL-25 alone or in combination with IFN-γ neutralization on ILC2 biology and disease pathology. WT mice were treated with 3% DSS to induce colitis, followed by intraperitoneal injections of recombinant murine IL-25 (rmIL-25) and/or anti-IFN-γ antibody (anti-IFN-γ) (Fig. 3 U). Both rmIL-25 and anti-IFN-γ significantly reduced DAI scores, increased intestinal length, and decreased pathological scores compared with vehicle treatment (Fig. 3, V–Z). The combination of rmIL-25 and anti-IFN-γ showed the most pronounced effects. Flow cytometry analysis revealed that both treatments increased Xbp1s expression, ILC2 numbers, and the production of Areg, IL-5, and IL-13 (Fig. S4, F–I; and Fig. 3, AA–AC). ELISA confirmed effective neutralization of IFN-γ with anti-IFN-γ (Fig. S4 J). These findings highlight the critical roles of IL-25 and IFN-γ in regulating the Xbp1s pathway in ILC2s and demonstrate that modulating these cytokines can improve disease outcomes in DSS-induced colitis.

IL-25 and IFN-γ regulate IRE1α phosphorylation and *Xbp1* mRNA splicing in ILC2s via the p38 pathway

The activation of ILC2s driven by IL-25 involves extensive protein synthesis, including Areg, IL-5, and IL-13, which may lead to increased protein processing in the ER and consequent elevation of *Xbp1* mRNA splicing. To determine whether enhanced Xbp1s is simply a byproduct of increased protein synthesis, we treated ILC2s with cycloheximide (CHX), which inhibits translation elongation by blocking eIF2-mediated tRNA translocation (Schneider-Poetsch et al., 2010; Siegel and Sisler, 1963), reducing the influx of newly synthesized proteins and alleviating ER stress (Xu and Wang, 2024). Flow cytometry analysis confirmed that CHX treatment significantly inhibited the production of Areg, IL-5, and IL-13 in ILC2s (Fig. 4, A and B). However, despite this inhibition, the spliced form of *Xbp1* remained unaltered following CHX treatment (Fig. 4 C), suggesting that *Xbp1* mRNA splicing is induced by IL-25 independently of enhanced protein processing. This observation suggests that *Xbp1* mRNA splicing is an upstream event in ILC2 effector molecule production, rather than a secondary response to enhanced protein translation.

Next, we aimed to elucidate the downstream pathways of IL-25 that contribute to *Xbp1* splicing in ILC2s. Given that IL-25 can

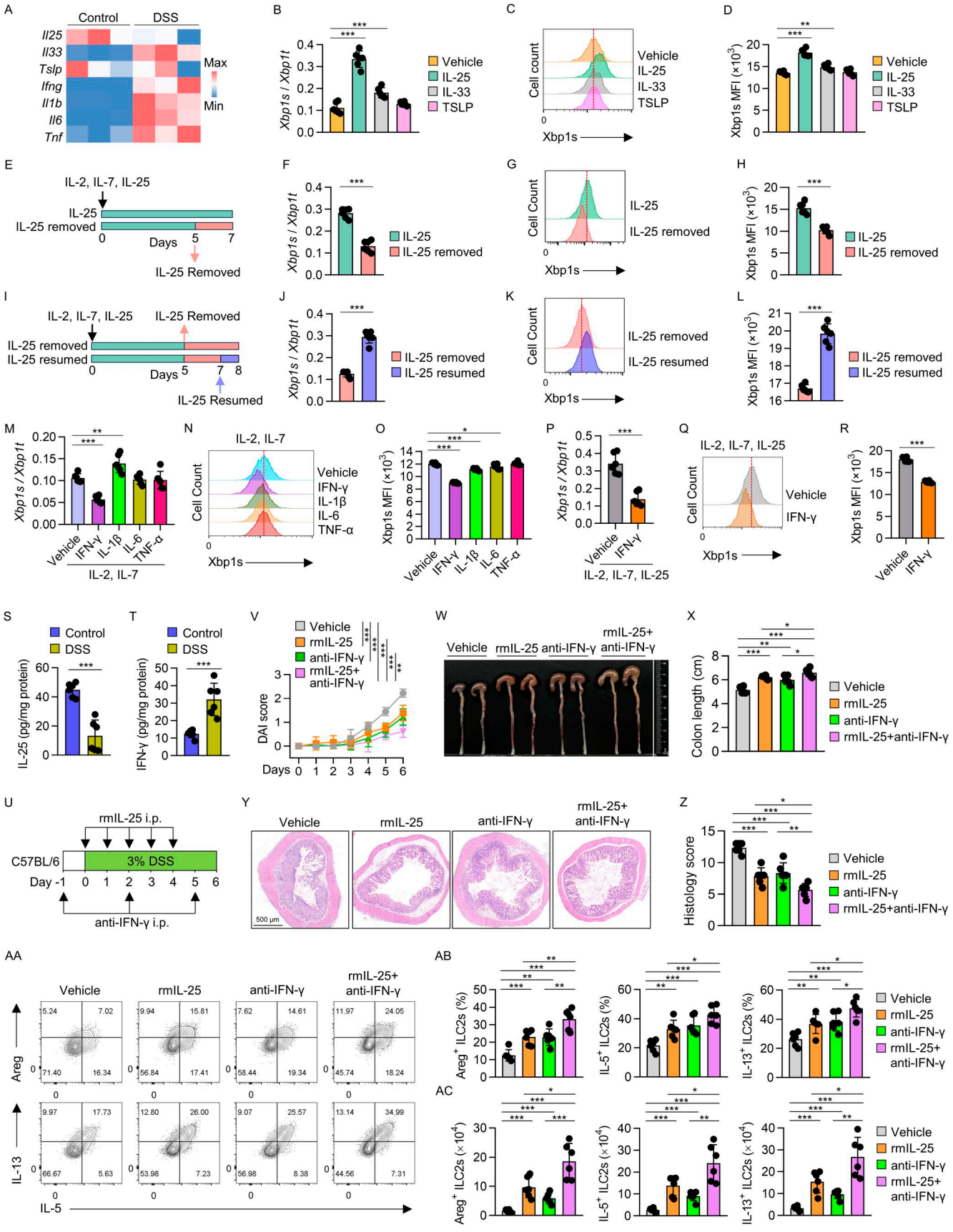

Figure 3. **IL-25 and the pro-inflammatory cytokine IFN-γ affect ILC2 function by regulating *Xbp1* mRNA splicing. (A)** Heatmap of ILC2s activator genes and pro-inflammatory genes by conducting RNA-seq analysis with mid-colon tissues of mice treated with 3% DSS for 6 days or control mice. The data are from

GSE210405, previously published by our team. **(B–D)** Sorted ILC2s ($Lin^-CD127^+KLRG1^+$) were cultured in complete IMDM containing IL-2 (10 ng/ml) and IL-7 (10 ng/ml), and co-incubated for 16 h with IL-25 (10 ng/ml), IL-33 (10 ng/ml), or TSLP (10 ng/ml), respectively. *Xbp1* mRNA splicing in ILC2s was detected using qRT-PCR (B). *Xbp1s*, spliced form of *Xbp1*. *Xbp1t*, total *Xbp1*. Analysis of Xbp1s expression in ILC2s ($CD45.2^+Lin^-GATA3^+$) by flow cytometry (C). MFI of Xbp1s (D) in indicated groups. Data were compiled from two independent experiments. Data are shown as the mean ± SD (n = 6 per group). **(E–H)** Sorted ILC2s ($Lin^-CD127^+KLRG1^+$) were cultured in complete IMDM containing IL-2, IL-7, and IL-25 (10 ng/ml each) for 5 days. Subsequently, the IL-25 was removed for 2 days. Experimental design (E). *Xbp1* mRNA splicing of indicated ILC2s was detected by qRT-PCR (F). Xbp1s expression in ILC2s ($CD45.2^+Lin^-GATA3^+$) was determined by flow cytometry (G), MFI of Xbp1s in ILC2s (H). Data were compiled from two independent experiments. Data are shown as the mean ± SD (n = 6 per group). **(I–L)** Sorted ILC2s ($Lin^-CD127^+KLRG1^+$) were cultured in complete IMDM containing IL-2, IL-7, and IL-25 (10 ng/ml each) for 5 days, and IL-25 was removed for 2 days, followed by restimulation with or without IL-25 (10 ng/ml) for 1 day. Experimental design (I). *Xbp1* mRNA splicing of indicated ILC2s was detected by qRT-PCR (J). Analysis of Xbp1s expression in ILC2s ($CD45.2^+Lin^-GATA3^+$) by flow cytometry (K). MFI of Xbp1s in ILC2s (L). Data were compiled from two independent experiments. Data are shown as the mean ± SD (n = 6 per group). **(M–O)** Sorted ILC2s ($Lin^-CD127^+KLRG1^+$) were cultured in complete IMDM containing IL-2 (10 ng/ml) and IL-7 (10 ng/ml), and co-incubated for 3 days with IFN-γ (50 ng/ml), IL-1β (50 ng/ml), IL-6 (50 ng/ml), or TNF-α (50 ng/ml), respectively. *Xbp1* mRNA splicing in ILC2s was detected using qRT-PCR (M). Analysis of Xbp1s expression in ILC2s ($CD45.2^+Lin^-GATA3^+$) by flow cytometry (N). MFI of Xbp1s in ILC2s (O). Data were compiled from two independent experiments. Data are shown as the mean ± SD (n = 6 per group). **(P–R)** Sorted ILC2s ($Lin^-CD127^+KLRG1^+$) were stimulated with the IFN-γ (500 ng/ml) for 3 days in complete IMDM containing IL-2, IL-7, and IL-25 (10 ng/ml each). *Xbp1* mRNA splicing of ILC2s was detected using qRT-PCR (P). Analysis of Xbp1s expression in ILC2s ($CD45.2^+Lin^-GATA3^+$) by flow cytometry (Q). MFI of Xbp1s in ILC2s (R). Data were compiled from two independent experiments. Data are shown as the mean ± SD (n = 6 per group). **(S and T)** After inducing colitis in WT mice with 3% DSS in drinking water for 6 days, the concentrations of IL-25 (S) and IFN-γ (T) in colon tissues were measured by ELISA. Data were compiled from two independent experiments. Data are shown as the mean ± SD (n = 6 per group). **(U–AC)** WT mice were administered 3% DSS in drinking water for 6 days to induce colitis, rmIL-25 (0.4 μg) was injected i.p. five doses daily from the onset of colitis induction, while anti-IFN-γ (1 mg) was injected i.p. on days −1, 2, and 5; the mice were sacrificed for analysis on day 6. Experimental design (U). DAI scores (V) were monitored at the indicated time points. Representative large intestine images (W). Lengths of colons (X). Representative H&E staining of the colon. Scale bar, 500 μm (Y). Histological severity scores of colons (Z). Flow cytometry analysis of Areg, IL-5, and IL-13 expression in large intestinal ILC2s ($CD45.2^+Lin^-GATA3^+$) (AA). Percentages (AB) and absolute numbers (AC) of $Areg^+$, $IL\text{-}5^+$, and $IL\text{-}13^+$ ILC2s. Data were compiled from two independent experiments and are shown as the mean ± SD (n = 6 per group). *P < 0.05, **P < 0.01, ***P < 0.001.

activate multiple signaling networks, including JNK, ERK, p38, and NF-κB (Fig. 4 D), we treated *in vitro*–cultured ILC2s with inhibitors targeting these pathways in the presence of IL-25. Our findings revealed that among these inhibitors, only PH797804, a selective inhibitor of p38, suppressed IL-25–induced *Xbp1* mRNA splicing and Xbp1s protein levels (Fig. 4, E–G), as well as IL-25–driven Areg, IL-5, and IL-13 production in ILC2s (Fig. 4, H and I). *Xbp1* mRNA is spliced by phosphorylated IRE1α (p-IRE1α) (Ali et al., 2011; Walter and Ron, 2011). Western blotting showed that inhibition of p38 with PH797804 markedly reduced the levels of p-IRE1α, as well as Xbp1s protein levels in sorted ILC2s treated with IL-25 (Fig. 4 J). Western blotting demonstrated that IL-25 markedly increased the expression of phosphorylated p38 (p-p38) (Fig. 4 K). Of note, the IFN-γ treatment led to a notable decrease in p-p38 levels within ILC2s (Fig. 4 L). These results suggest that IL-25 enhances *Xbp1* mRNA splicing in gut ILC2s by activating the p38-IRE1α phosphorylation axis, whereas IFN-γ inhibits this pathway, highlighting the opposing regulatory effects of IL-25 and IFN-γ on colonic ILC2s.

Xbp1s directs the expression of dihydrofolate reductase, a key enzyme in folate cycle

Upon translation, the spliced form of Xbp1, Xbp1s, acts as a transcription factor. To elucidate how Xbp1 signaling influences gut ILC2s at a molecular level, we employed cleavage under targets and tagmentation with high-throughput sequencing (CUT&Tag-seq) using an antibody against Xbp1s to explore the genome-wide occupancy of Xbp1s on chromatin. Analysis of Xbp1s-binding signals revealed a total of 1,070 bound genes in ILC2s, predominantly distributed across gene promoter regions (64%, ≤1 kb) and intergenic regions (11.31%) (Fig. 5 A; Fig. S4, K–M; and Table S5). Notably, among the genes encoding ILC2 effector molecules, such as *Il5*, *Il13*, and *Areg*, only *Il13* exhibited a binding peak with Xbp1s, while *Il5* and *Areg* did not, suggesting that Xbp1s indirectly regulates intestinal ILC2s (Table S5). KEGG pathway enrichment analysis indicated that the target genes of Xbp1s were primarily associated with pathways linked to protein processing in ER and protein export, consistent with the established biological role of Xbp1s (Fig. S5 A).

Integrating Xbp1s-binding genes identified by CUT&Tag-seq with DEGs due to toyocamycin treatment in gut ILC2s revealed 407 overlapping genes with altered mRNA levels upon inhibition of *Xbp1* mRNA splicing (Fig. 5 A and Table S6). Among the overlapping genes, 203 were downregulated and 204 were upregulated in toyocamycin-treated ILC2s, with *Dhfr* that encodes dihydrofolate reductase (DHFR), being one of the most significantly decreased genes (Fig. 5 B, Fig. S5 B, and Table S6). Accordingly, CUT&Tag-seq analysis revealed direct binding of Xbp1s to the promoter region of *Dhfr* (Fig. 5 C). To further confirm Xbp1s direct role in promoting *Dhfr* transcription, we conducted a luciferase reporter assay. Xbp1s markedly enhanced *Dhfr* promoter–driven luciferase activity, and this effect was abolished in the *Dhfr* promoter mutant lacking the Xbp1s-binding region (Fig. 5, D and E).

Western blotting revealed that IL-25, which promotes *Xbp1* mRNA splicing, elevated the levels of the DHFR protein (Fig. 5 F). In addition, inhibition of Xbp1s with toyocamycin reduced the protein levels of DHFR (Fig. 5 G), and IL-25–induced elevation of DHFR was suppressed by IFN-γ or the p38 inhibitor PH797804 in ILC2s (Fig. 5 H and Fig. S5 C). Of note, in line with impaired ILC2s in DSS-induced colitis, we observed decreased *Dhfr* mRNA levels in ILC2s from DSS-treated mice compared with control mice (Fig. S5 D). Additionally, *Dhfr* mRNA levels were markedly reduced in ILC2s from $Xbp1^{f/f}Il5^{RFP\text{-}Cre}$ mice compared with those from $Xbp1^{+/+}Il5^{RFP\text{-}Cre}$ control mice (Fig. S5 E).

We sought to investigate the potential role of DHFR in colonic ILC2 function. Treatment of sorted gut ILC2s with methotrexate (MTX), a potent antagonist of DHFR, reduced ILC2 viability and

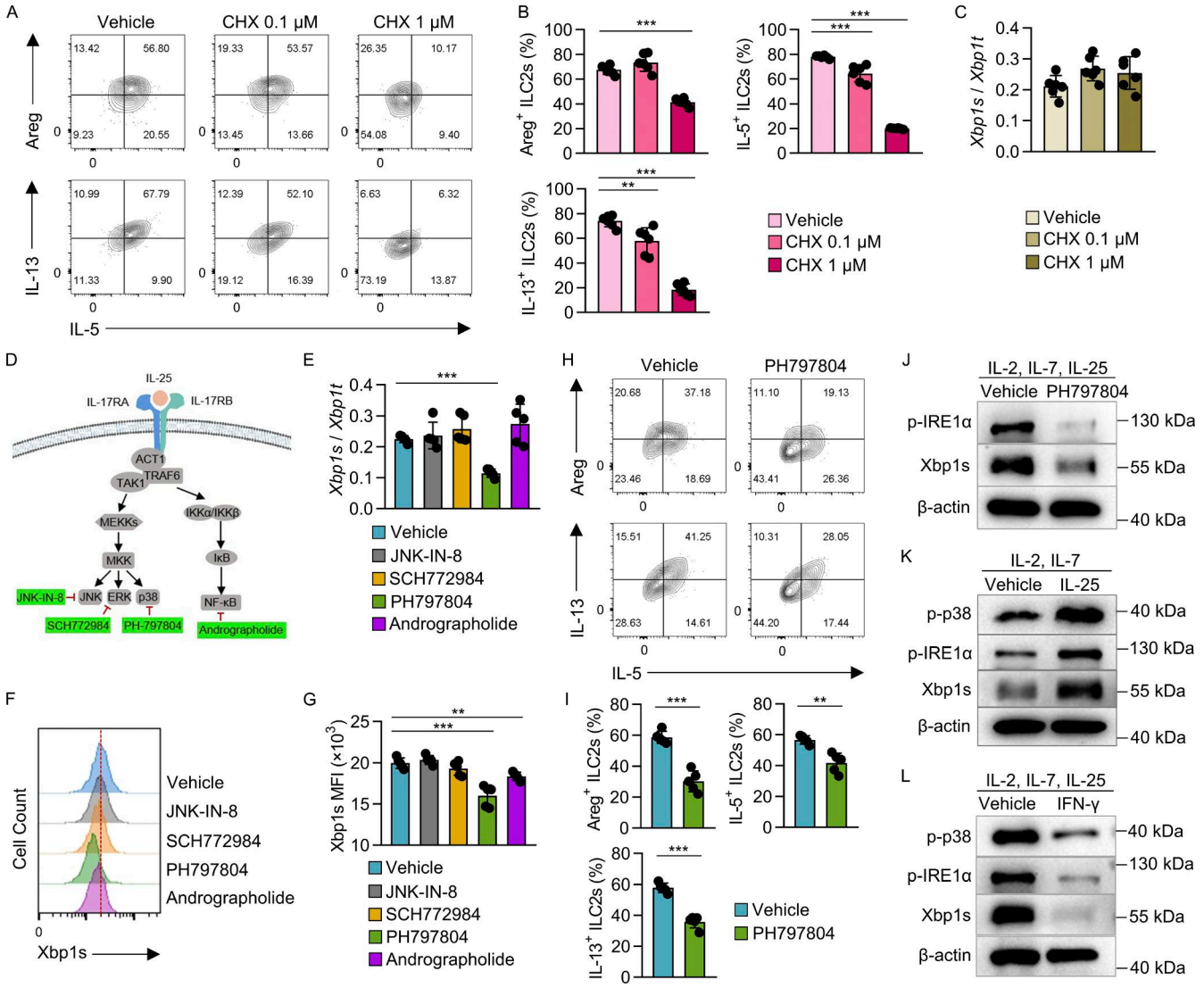

Figure 4. **IL-25 and IFN-γ regulate *Xbp1* mRNA splicing in ILC2s through p38-mediated IRE1α phosphorylation. (A–C)** Sorted ILC2s (Lin⁻CD127⁺KLRG1⁺) were cultured in complete IMDM containing IL-2, IL-7, and IL-25 (10 ng/ml each) for 5 days, followed by treatment with CHX at the indicated concentrations for 2 days. Areg, IL-5, and IL-13 expressions in ILC2s (CD45.2⁺Lin⁻GATA3⁺) were analyzed by flow cytometry (A). Percentages of Areg⁺, IL-5⁺, and IL-13⁺ cells in ILC2s (B). *Xbp1* mRNA splicing of ILC2s was detected by qRT-PCR (C). Data were compiled from two independent experiments. Data are shown as the mean ± SD (n = 6 per group). **(D–G)** Sorted ILC2s (Lin⁻CD127⁺KLRG1⁺) were stimulated with the inhibitors of IL-25 downstream signaling pathways for 16 h, including JNK-IN-8 (10 μM), SCH772984 (1 μM), PH797804 (10 μM), and andrographolide (10 μM) as shown in D. *Xbp1* mRNA splicing of ILC2s was detected by qRT-PCR (E). Xbp1s expression in ILC2s (CD45.2⁺Lin⁻GATA3⁺) was analyzed by flow cytometry (F). MFI of Xbp1s in ILC2s (G). Data were compiled from two independent experiments. Data are shown as the mean ± SD (n = 5 per group). **(H and I)** Sorted ILC2s (Lin⁻CD127⁺KLRG1⁺) were stimulated with PH797804 (10 μM) for 16 h in complete IMDM containing IL-2, IL-7, and IL-25 (10 ng/ml each). Analysis of Areg, IL-5, and IL-13 expression in ILC2s (CD45.2⁺Lin⁻GATA3⁺) by flow cytometry (H). Percentages of Areg⁺, IL-5⁺, and IL-13⁺ cells in ILC2s (I). Data were compiled from three independent experiments. Data are shown as the mean ± SD (n = 5 per group). **(J)** Sorted ILC2s (Lin⁻CD127⁺KLRG1⁺) were cultured for 5 days, followed by PH797804 treatment at 10 μM for 16 h. The level of p-IRE1α and Xbp1s in ILC2s was detected by western blotting. β-Actin served as the internal control. Data are representative of three independent experiments. **(K)** Sorted ILC2s (Lin⁻CD127⁺KLRG1⁺) were cultured for 5 days in the presence of IL-2, IL-7, and IL-25 (10 ng/ml each), and IL-25 was removed for 2 days, followed by re-stimulation with or without IL-25 (10 ng/ml) for 1 day. The level of p-p38, p-IRE1α, and Xbp1s in ILC2s was analyzed by western blotting. β-Actin served as the internal control. Data are representative of three independent experiments. **(L)** Sorted ILC2s (Lin⁻CD127⁺KLRG1⁺) were stimulated with the IFN-γ (500 ng/ml) for 3 days in complete IMDM containing IL-2, IL-7, and IL-25 (10 ng/ml each). Expression of p-p38, p-IRE1α, and Xbp1s in ILC2s was analyzed by western blotting. β-Actin served as the internal control. Data are representative of three independent experiments. **P < 0.01, ***P < 0.001. Source data are available for this figure: SourceData F4.

suppressed the production of Areg, IL-5, and IL-13 (Fig. S5, F–H; and Fig. 5 I). Furthermore, decreased *DHFR* mRNA levels were observed in amplified human ILC2s following toyocamycin treatment, which extends the regulation of DHFR by Xbp1s in mouse ILC2s to human ILC2s (Fig. 5 J). Notably, treatment of human LPMNCs with the DHFR inhibitor MTX led to a reduction in AREG expression in colonic ILC2s (Fig. 5, K and L). Conversely, forced expression of DHFR in sorted intestinal ILC2s restored the levels of Areg, IL-5, and IL-13 following inhibition of *Xbp1* mRNA splicing by toyocamycin (Fig. 5, M–P), suggesting

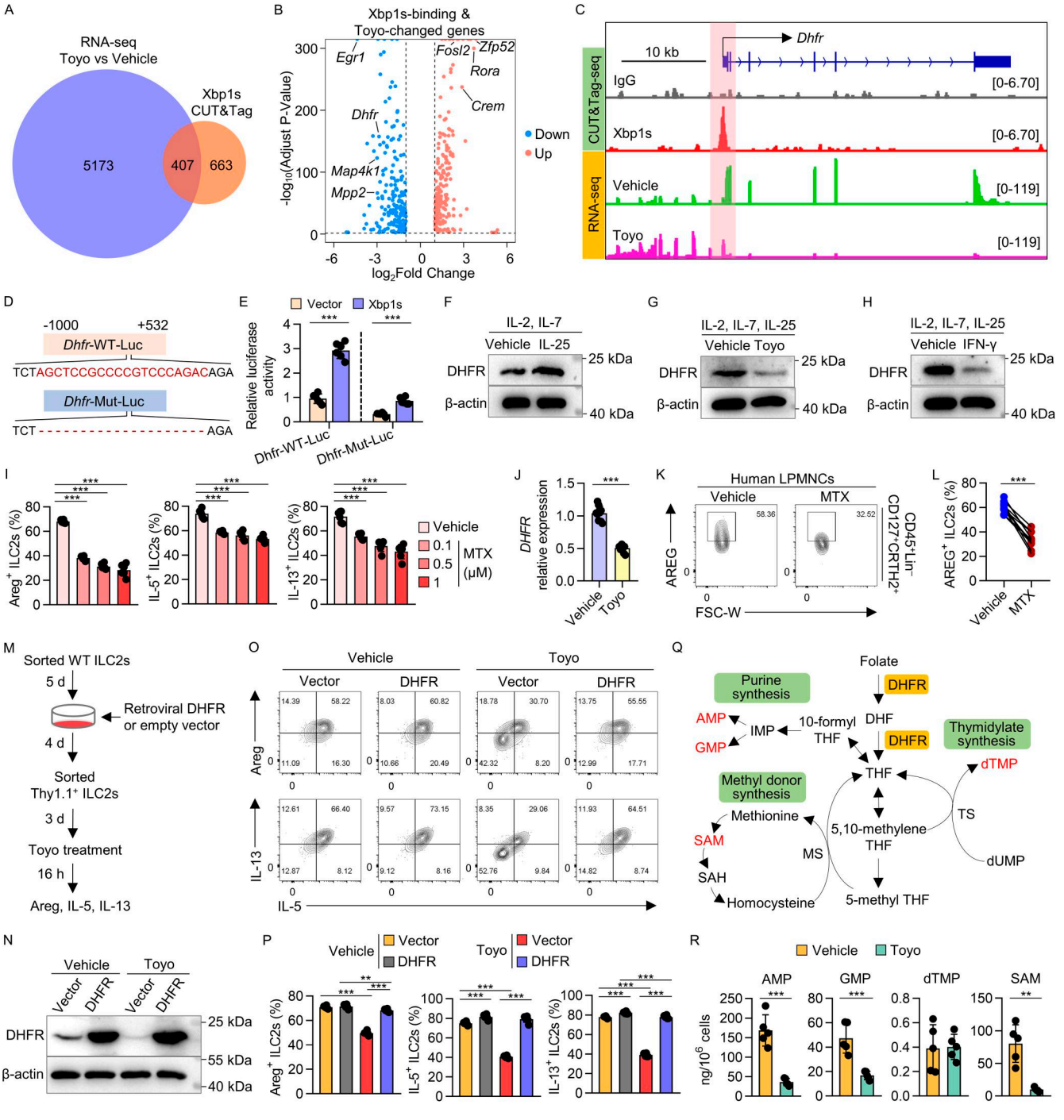

Figure 5. **Xbp1s governs colonic ILC2s by targeting DHFR. (A)** Venn diagram showed the numbers of overlapping genes between Xbp1s bindings in CUT&Tag-seq (FDR < 0.01) and DEGs in RNA-seq (log_2[fold change] >1 or less-than −1, FDR < 0.01) of ILC2s after treated with Toyo at 4 μM. **(B)** Volcano plot of overlapping genes described in Fig. 5 A. **(C)** Recruitment of Xbp1s to the *Dhfr* locus in ILC2s by analyzing CUT&Tag-seq data (upper). Representative RNA-seq tracks at the *Dhfr* locus in indicated ILC2s (bottom). **(D and E)** Putative Xbp1s-responsive element in the *Dhfr* promoter (D). Luciferase activity of a *Dhfr* wild-type promoter reporter (*Dhfr*-WT-Luc) or of a *Dhfr* mutant reporter (*Dhfr*-Mut-Luc) containing a deletion in the Xbp1s-responsive element in HEK293T cells transiently expressing either vector (pcDNA3.1) or Xbp1s. Data were compiled from two independent experiments. Data are shown as the mean ± SD (n = 6 per group). **(F)** Sorted ILC2s (Lin$^-$CD127$^+$KLRG1$^+$) were cultured for 5 days in the presence of IL-2, IL-7, and IL-25 (10 ng/ml each), and IL-25 was removed for 2 days, followed by restimulation with or without IL-25 (10 ng/ml) for 1 day. The level of DHFR in ILC2s was detected by western blotting. β-Actin served as the internal control. Data are representative of three independent experiments. **(G)** Sorted ILC2s (Lin$^-$CD127$^+$KLRG1$^+$) were cultured for 5 days in the presence of IL-2, IL-7, and IL-25 (10 ng/ml each), followed by treatment with Toyo at 4 μM for 16 h. The level of DHFR in indicated ILC2s was detected by western blotting. β-Actin served as the internal control. Data are representative of three independent experiments. **(H)** Sorted ILC2s (Lin$^-$CD127$^+$KLRG1$^+$) were stimulated with the IFN-γ (500 ng/ml) for 3 days in complete IMDM containing IL-2, IL-7, and IL-25 (10 ng/ml each). The level of DHFR in indicated ILC2s was detected by western blotting. β-Actin served as the internal control. Data are representative of three independent experiments. **(I)** Sorted ILC2s (Lin$^-$CD127$^+$KLRG1$^+$) were cultured in the presence of IL-2, IL-7, and IL-25 (10 ng/ml each), with or without MTX co-incubation for 3 days at the indicated concentrations. Percentages of Areg$^+$, IL-5$^+$, and

IL-13$^+$ ILC2s (CD45.2$^+$Lin$^-$GATA3$^+$) were analyzed by flow cytometry. Data were compiled from two independent experiments. Data are shown as the mean ± SD (n = 6 per group). **(J)** Purified human peripheral blood ILC2s were cultured for 3 wk in the presence of hIL-2, hIL-7, hIL-25, and hIL-33 (20 ng/ml each), followed by treatment with Toyo at 25 nM for 16 h. *DHFR* mRNA expression in ILC2s was detected by qRT-PCR. Data are shown as the mean ± SD (n = 10 per group). **(K and L)** Human colonic LPMNCs were stimulated with the MTX at 20 μM for 16 h in complete RPMI 1640 medium. AREG expression in ILC2s (CD45$^+$Lin$^-$CD127$^+$CRTH2$^+$) was analyzed by flow cytometry (K). Percentage of AREG$^+$ ILC2s (L). Connected lines are samples from the same clinical samples (n = 10). P value was determined by two-tailed paired Student's t test. **(M–P)** Large intestinal ILC2s (Lin$^-$CD127$^+$KLRG1$^+$) were sorted from WT mice and underwent retroviral transduction of DHFR with IRES-controlled Thy1.1 expression to label transduced cells. Thy1.1$^+$ cells after gating on Lin$^-$CD45.2$^+$ were sorted and cultured for 3 days, followed by treatment with Toyo at 4 μM for 16 h. Experimental design (M). Levels of DHFR protein in indicated ILC2s were detected by western blotting (N). β-Actin served as the internal control. Flow cytometry analyses of Areg, IL-5, and IL-13 expression in the ILC2s (CD45$^+$Lin$^-$GATA3$^+$) (O). Percentages of Areg$^+$, IL-5$^+$, and IL-13$^+$ ILC2s (P). Data were compiled from two independent experiments. Data are shown as the mean ± SD (n = 6 per group). **(Q)** Schematic diagram of folate-dependent 1C metabolic pathways, including representative enzymes and metabolic products. **(R)** Sorted large intestinal ILC2s (Lin$^-$CD127$^+$KLRG1$^+$) were cultured for 5 days, and then incubated with or without Toyo at 4 μM for 16 h. Levels of folate-derived metabolites AMP, GMP, dTMP, and SAM were detected by HPLC-MS/MS (n = 5 per group). **P < 0.01, ***P < 0.001. FDR, false discovery rate. Source data are available for this figure: SourceData F5.

that DHFR acts as a downstream target of Xbp1s, mediating its impact on ILC2s in the gut.

Xbp1s orchestrates folate-mediated 1C metabolism to sustain gut ILC2s

DHFR assumes a pivotal role in the folate cycle, critical for 1C metabolism responsible for synthesizing thymidylate, purine, and methyl donors (Fig. 5 Q). This prompted us to hypothesize that Xbp1s modulates DHFR, thereby influencing downstream metabolites of 1C metabolism to regulate intestinal ILC2s. Utilizing high-performance liquid chromatography–mass spectrometry/mass spectrometry (HPLC-MS/MS), we quantitatively analyzed terminal derivatives in 1C metabolism from sorted ILC2s treated with toyocamycin or vehicle control, including AMP, guanosine 5′-monophosphate (GMP), 2′-deoxythymidine-5′-monophosphate (dTMP), and S-adenosyl methionine (SAM). The results unveiled significant reductions in AMP, GMP, and SAM levels in toyocamycin-treated ILC2s, while dTMP remained unaffected (Fig. 5 R). Additionally, metabolomics analysis showed marked reductions in a series of metabolites associated with 1C metabolism, including folinic acid, methionine, SAM, SAH, cysteine, serine, and glycine (Fig. S5 I). To elucidate the impact of the terminal derivatives on the regulation of gut ILC2s by Xbp1s, we supplemented toyocamycin-treated ILC2s with these metabolites. Flow cytometry analysis demonstrated that AMP notably restored the production of Areg, IL-5, and IL-13 in toyocamycin-treated ILC2s, with SAM showing a modest restoration effect (Fig. 6, A and B). Conversely, dTMP and GMP failed to counteract the inhibitory effect of reduced *Xbp1* splicing (Fig. 6, A and B). In accordance, AMP supplementation in toyocamycin-treated human LPMNCs restored the production of AREG in human colonic ILC2s (Fig. 6, C and D).

While AMP primarily serves as a provider of purine bases for DNA and RNA synthesis, it can also be converted into the second messenger cAMP by adenylate cyclase (AC). Considering the indispensable role of cAMP in sustaining ILC2 function, the AC-specific inhibitor SQ22536 was administered in the context of AMP restoring the compromised function of ILC2s caused by *Xbp1* mRNA splicing inhibitor, toyocamycin (Fig. S5 J). We observed that adding SQ22536 attenuated AMP's ability to restore the production of Areg, IL-5, and IL-13 in toyocamycin-treated ILC2s, underscoring the essential role of AMP-derived cAMP in maintaining ILC2 effector function (Fig. 6, E and F).

Notably, cAMP has been shown to inhibit ILC2 function in various contexts, but its effects specifically under IL-25 stimulation are less clear (Nagashima et al., 2019; Wallrapp et al., 2019; Xu et al., 2019; Zhou et al., 2018). In fact, inhibiting cAMP production with SQ22536 reduced Areg, IL-5, and IL-13 levels in IL-25–stimulated ILC2s, but showed minimal effect on these effector molecules in IL-33–treated ILC2s (Fig. S5, K and L). These findings suggest that different stimuli may activate distinct signaling pathways in ILC2s, leading to variable responses to cAMP. Supporting this, recent reports indicate that IL-33, rather than IL-25, activates lipid metabolism in lung ILC2s (Rao et al., 2024).

In addition to the scenario of pharmacological Xbp1s inhibition by toyocamycin, AMP supplementation also restored effector molecule production in *Xbp1*-deficient ILC2s (Fig. 6, G and H). Furthermore, we showed that forced expression of DHFR rescued the production of Areg, IL-5, and IL-13 in *Xbp1*-deleted ILC2s (Fig. 6, I–K; and Fig. S5 M). Overall, our data suggest that Xbp1s regulates DHFR expression to sustain AMP generation from folate-fueled 1C metabolism, thereby directing the function of intestinal ILC2s.

Of note, Xbp1s plays a pivotal role in lipid metabolism by regulating processes such as cholesterol and fatty acid biosynthesis within the ER in multiple cell types (Casali et al., 2020; Cubillos-Ruiz et al., 2015; Sha et al., 2009; Wang et al., 2022; Yang et al., 2022). Accordingly, our CUT&Tag-seq analysis revealed that Xbp1s in gut ILC2s bound to the promoter region of *Srebf2* (Fig. S5 N), which encodes sterol regulatory element-binding protein 2 (Srebp2), a key regulator of cholesterol and fatty acid synthesis (Branche et al., 2022; Guo et al., 2018; Madison, 2016). To test whether cholesterol or fatty acid participates in the regulation of gut ILC2s by Xbp1s, we supplemented toyocamycin-treated ILC2s with cholesterol or palmitic acid. Flow cytometry analysis indicated that neither cholesterol nor palmitic acid restored the production of Areg, IL-5, and IL-13 in ILC2s with diminished *Xbp1* mRNA splicing induced by toyocamycin (Fig. S5, O and P).

AMP derived from 1C metabolism restrains the progression of DSS-induced colitis

Given the essential role of Xbp1-directed 1C metabolite AMP in facilitating gut ILC2s to produce effector molecules crucial for intestinal tissue repair during colitis, we sought to investigate

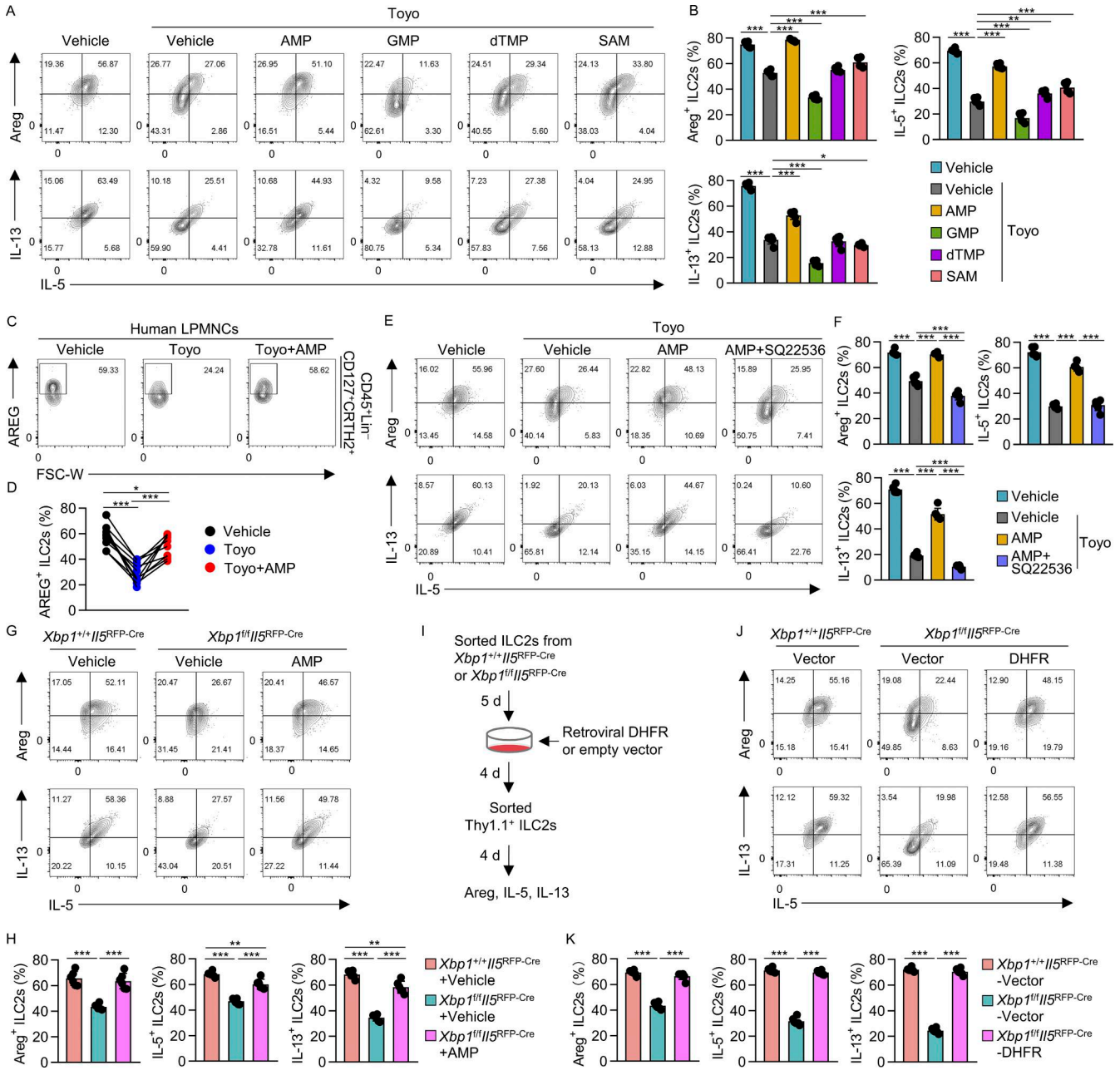

Figure 6. **Xbp1s directs DHFR expression, orchestrating 1C metabolism to sustain gut ILC2s. (A and B)** Sorted large intestinal ILC2s (Lin$^-$CD127$^+$KLRG1$^+$) were cultured in the presence of IL-2, IL-7, IL-25 (10 ng/ml each) for 5 days, followed by treatment with Toyo at 4 µM, with or without AMP, GMP, dTMP, and SAM (1 mM each) for 16 h. Flow cytometry analysis of Areg, IL-5, and IL-13 expression in ILC2s (CD45.2$^+$Lin$^-$GATA3$^+$) (A). Percentages of Areg$^+$, IL-5$^+$, and IL-13$^+$ ILC2s (B). Data were compiled from two independent experiments. Data are shown as the mean ± SD (n = 6 per group). **(C and D)** Human colonic LPMNCs were stimulated with Toyo at 25 µM, supplemented with or without AMP for 16 h in complete RPMI 1640 media. AREG expression was analyzed after gating on CD45$^+$Lin$^-$CD127$^+$CRTH2$^+$ ILC2s (C). Percentage of AREG$^+$ ILC2s (D). Connected lines are samples from the same clinical samples (n = 10). P value was determined by two-tailed paired Student's t test. **(E and F)** Sorted large intestinal ILC2s (Lin$^-$CD127$^+$KLRG1$^+$) were cultured in the presence of IL-2, IL-7, IL-25 (10 ng/ml each) for 5 days, followed by treatment with Toyo at 4 µM, and then supplemented with or without AMP (1 mM), and SQ22536 (1 mM), a potent inhibitor of AC. Flow cytometry analysis of Areg, IL-5, and IL-13 expression in ILC2s (CD45.2$^+$Lin$^-$GATA3$^+$) (E). Percentages of Areg$^+$, IL-5$^+$, and IL-13$^+$ ILC2s (F). Data were compiled from two independent experiments. Data are shown as the mean ± SD (n = 6 per group). **(G and H)** Sorted large intestinal ILC2s (Lin$^-$CD127$^+$KLRG1$^+$) from *Xbp1*$^{+/+}$*Il5*$^{RFP\text{-}Cre}$ and *Xbp1*$^{f/f}$*Il5*$^{RFP\text{-}Cre}$ mice were cultured in the presence of IL-2, IL-7, IL-25 (10 ng/ml each) for 5 days; the ILC2s from *Xbp1*$^{f/f}$*Il5*$^{RFP\text{-}Cre}$ mice were incubated with AMP (1 mM) for 16 h. Flow cytometry analyses of Areg, IL-5, and IL-13 expression after gating on CD45.2$^+$Lin$^-$GATA3$^+$ ILC2s (G). Percentages of Areg$^+$, IL-5$^+$, and IL-13$^+$ ILC2s (H). Data were compiled from two independent experiments. Data are shown as the mean ± SD (n = 6 per group). **(I–K)** Large intestinal ILC2s (Lin$^-$CD127$^+$KLRG1$^+$) were sorted from *Xbp1*$^{f/f}$*Il5*$^{RFP\text{-}Cre}$ or littermate *Xbp1*$^{+/+}$*Il5*$^{RFP\text{-}Cre}$ mice and underwent retroviral transduction of DHFR with IRES-controlled Thy1.1 expression to label transduced cells. Thy1.1$^+$ cells after gating on Lin$^-$CD45.2$^+$ were sorted and cultured for 4 days. Experimental design (I). Flow cytometry analysis of Areg, IL-5, and IL-13 expression in ILC2s (CD45$^+$Lin$^-$GATA3$^+$) (J). Percentages of Areg$^+$, IL-5$^+$, and IL-13$^+$ ILC2s (K). Data were compiled from two independent experiments. Data are shown as the mean ± SD (n = 6 per group). *P < 0.05, **P < 0.01, ***P < 0.001.

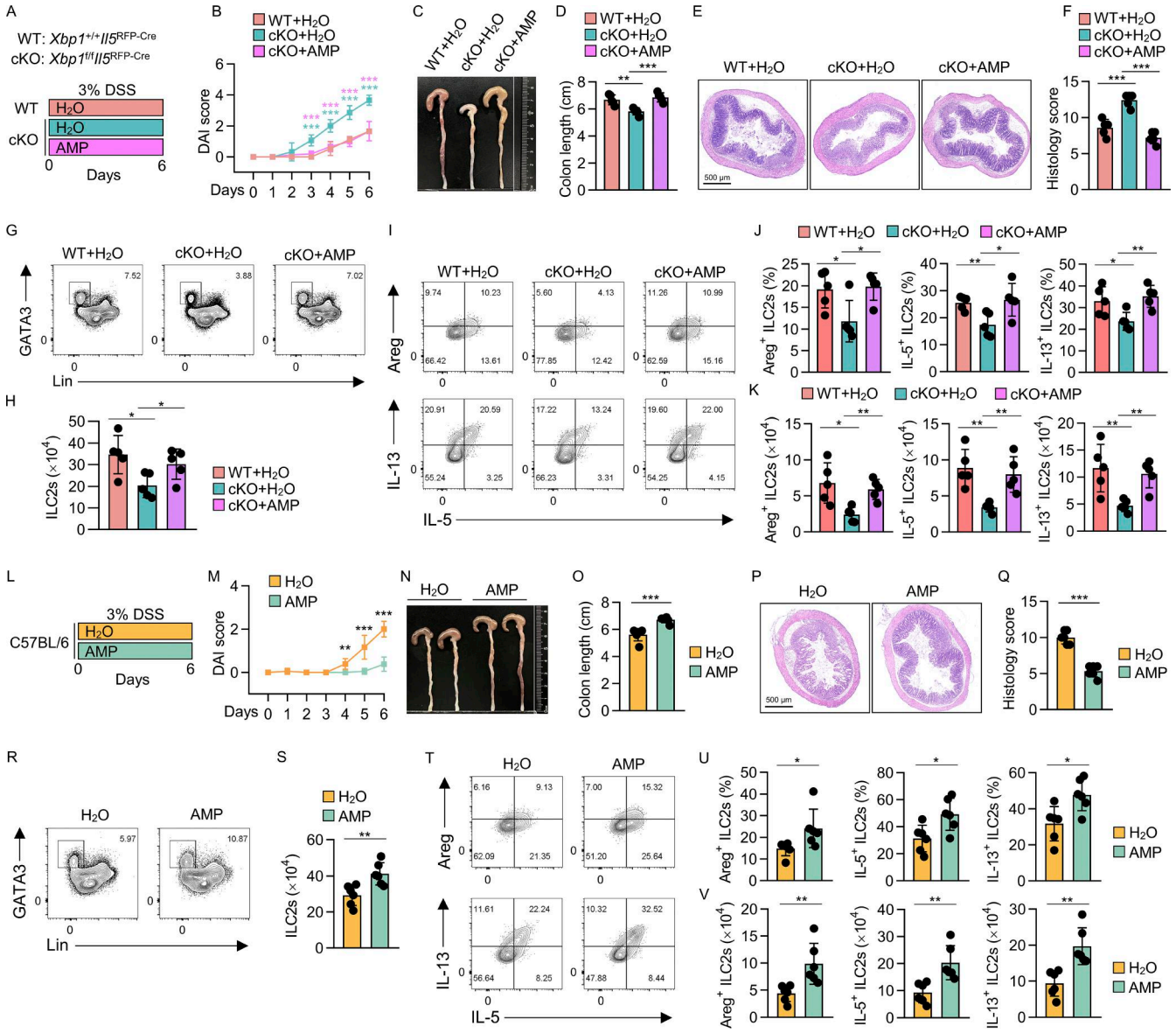

Figure 7. **AMP derived from 1C metabolism restrains the progression of DSS-induced colitis by promoting ILC2 function. (A–K)** WT (*Xbp1*$^{+/+}$*Il5*$^{RFP\text{-}Cre}$) or cKO (*Xbp1*$^{f/f}$*Il5*$^{RFP\text{-}Cre}$) mice were gavaged with H_2O or AMP (800 mg/kg) at day 0 to day 5 during 3% DSS treated for 6 days. Experimental design (A). DAI scores (B) were monitored every day during the experiments. The blue asterisk represents the comparison between the WT and cKO groups; the purple asterisk represents the comparison between the cKO+H_2O and cKO+AMP groups. Representative large intestine images (C). Lengths of colons (D). Representative H&E staining of the colon. Scale bar, 500 µm (E). Histological severity scores of colons (F). Flow cytometry analysis of GATA3 expression after gating on CD45.2$^+$Lin$^-$ cells in large intestinal LPLs (G). Absolute numbers of ILC2s (CD45.2$^+$Lin$^-$GATA3$^+$) (H). Flow cytometry analysis of Areg, IL-5, and IL-13 expression in ILC2s (I). Percentages (J) and absolute numbers (K) of Areg$^+$, IL-5$^+$, and IL-13$^+$ ILC2s. Data were compiled from three independent experiments. Data are shown as the mean ± SD (n = 5 per group). **(L–V)** WT mice were gavaged with H_2O or AMP (800 mg/kg) at day 0 to day 5 during 3% DSS administered for 6 days. Experimental design (L). DAI scores (M) were monitored at the indicated time points. Representative large intestine images (N). Lengths of colons (O). Representative H&E staining of the colon. Scale bar, 500 µm (P). Histology scores (Q). Flow cytometry analysis of GATA3 expression after gating on CD45.2$^+$Lin$^-$ cells in large intestinal LPLs (R). Absolute numbers of ILC2s (CD45.2$^+$Lin$^-$GATA3$^+$) (S). Flow cytometry analysis of Areg, IL-5, and IL-13 expression in ILC2s (T). Percentages (U) and absolute numbers (V) of Areg$^+$, IL-5$^+$, and IL-13$^+$ ILC2s. Data were compiled from two independent experiments. Data are shown as the mean ± SD (n = 6 per group). *P < 0.05, **P < 0.01, ***P < 0.001.

the impact of AMP on colitis progression. AMP administration, compared with vehicle control, attenuated aggravated colitis in *Xbp1*-cKO mice (Fig. 7, A–F), which was evidenced by reduced DAI scores, increased colon length, and improved histopathology (Fig. 7, B–F). Accordingly, the numbers of ILC2s and the production of Areg, IL-5, and IL-13 by colonic ILC2s were reduced in *Xbp1*$^{f/f}$*Il5*$^{RFP\text{-}cre}$ mice compared with those in *Xbp1*$^{+/+}$*Il5*$^{RFP\text{-}cre}$ control mice following DSS treatment, and this suppression in *Xbp1*$^{f/f}$*Il5*$^{RFP\text{-}cre}$ mice was significantly restored by AMP administration (Fig. 7, G–K).

Moreover, we found that AMP supplementation, compared with vehicle control, ameliorated DSS-induced colitis in WT

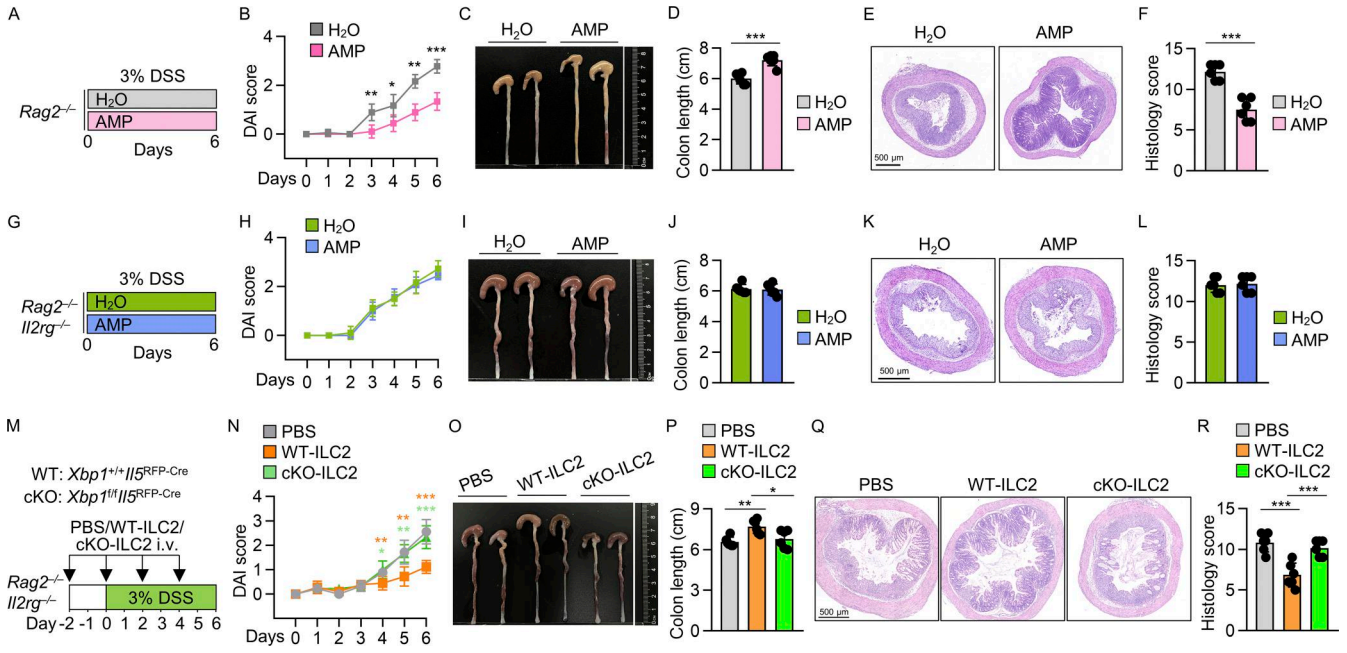

Figure 8. **AMP derived from Xbp1-mediated 1C metabolism restrains the progression of DSS-induced colitis in an ILC-dependent manner. (A–F)** *Rag2*$^{-/-}$ mice were gavaged with H_2O or AMP (800 mg/kg) at day 0 to day 5 during 3% DSS administered for 6 days. Experimental design (A). DAI scores (B) were monitored at the indicated time points. Representative large intestine images (C). Lengths of colons (D). Representative H&E histology sections of the colon. Scale bar, 500 µm (E). Histology scores (F). Data were compiled from two independent experiments and are shown as the mean ± SD (n = 6 per group). **(G–L)** *Rag2*$^{-/-}$*Il2rg*$^{-/-}$ mice were gavaged with H_2O or AMP (800 mg/kg) at day 0 to day 5 during 3% DSS treated for 6 days. Experimental design (G). DAI scores (H) were monitored every day during the experiments. Representative large intestine images (I). Lengths of colons (J). Representative H&E histology sections of the colon. Scale bar, 500 µm (K). Histology scores (L). Data were compiled from three independent experiments and are shown as the mean ± SD (n = 6 per group). **(M–R)** Sorted large intestinal ILC2s (Lin$^-$CD127$^+$KLRG1$^+$) from WT (*Xbp1*$^{+/+}$*Il5*$^{RFP\text{-}Cre}$) or cKO (*Xbp1*$^{f/f}$*Il5*$^{RFP\text{-}Cre}$) mice were transferred into *Rag2*$^{-/-}$*Il2rg*$^{-/-}$ mice during DSS-induced colitis. PBS was used as a vehicle control. Experimental design (M). DAI scores (N) were monitored at the indicated time points. The orange asterisk represents the comparison between the WT-ILC2 and PBS groups, and the green asterisk represents the comparison between the cKO-ILC2 and WT-ILC2 groups. Representative large intestine images (O). Lengths of colons (P). Representative H&E staining of the colon. Scale bar, 500 µm (Q). Histological severity scores of colons (R). Data were compiled from two independent experiments. Data are shown as the mean ± SD (n = 6 per group). *P < 0.05, **P < 0.01, ***P < 0.001.

mice (Fig. 7, L–Q). This pathological improvement was accompanied by increased ILC2 numbers and enhanced production of Areg, IL-5, and IL-13 by ILC2s in AMP-treated mice compared with controls (Fig. 7, R–V). Notably, AMP supplementation also alleviated colitis in *Rag2*$^{-/-}$ mice (Fig. 8, A–F), which lack T and B cells (Shinkai et al., 1992). However, it had no effect on disease progression in *Rag2*$^{-/-}$*Il2rg*$^{-/-}$ mice (Fig. 8, G–L), which lack T and B cells, as well as ILCs (Abt et al., 2015; Spolski et al., 2018). These findings suggest that the ability of 1C metabolism–derived AMP to restrain DSS-induced colitis progression is dependent on ILCs.

To further demonstrate the critical role of Xbp1 in ILC2s for alleviating colitis, we adoptively transferred colonic ILC2s isolated from *Xbp1*$^{+/+}$*Il5*$^{RFP\text{-}cre}$ or *Xbp1*$^{f/f}$*Il5*$^{RFP\text{-}cre}$ mice into *Rag2*$^{-/-}$*Il2rg*$^{-/-}$ mice, followed by DSS treatment to induce colitis. ILC2s sorted from *Xbp1*$^{+/+}$*Il5*$^{RFP\text{-}cre}$ mice significantly ameliorated colitis, whereas *Xbp1*-deficient ILC2s failed to confer protection (Fig. 8, M–R). Collectively, these results highlight the critical role of 1C metabolism, which relies on Xbp1-mediated regulation of DHFR in this pathway, for the protective function of gut ILC2s in colitis. Translationally, AMP administration holds promise as a therapeutic strategy for colitis.

Discussion

While the precise etiology of UC remains unclear, the accumulation of Xbp1s in the epithelial compartment of UC patients and experimental colitis models has been well documented. Previous studies have demonstrated that specific ablation of *Xbp1* in intestinal epithelial cells exacerbates DSS-induced colitis (Kaser et al., 2008), and IRE1α-Xbp1 signaling in epithelial cells may influence Th17 differentiation, contributing to the progression of inflammatory bowel disease (IBD) (Duan et al., 2023). However, the role of the IRE1α-Xbp1 axis within immune cell subsets responsible for tissue repair in UC has remained largely unexplored. In this study, we uncovered that gut ILC2s, pivotal for tissue repair, exhibit reduced *Xbp1* mRNA splicing during colitis, and that ILC2-specific deletion of *Xbp1* impairs their pro-repair functions, resulting in severe colitis. These findings highlight the critical role of the IRE1α-Xbp1 pathway in maintaining ILC2 function and underscore its potential as a therapeutic target for UC.

Of intriguing note, contradicting the worsened colitis seen with ILC2-specific *Xbp1* deletion in our study, recent findings indicate that IRE1α deletion, which is the upstream controller of *Xbp1* splicing, in ILC2s alleviates DSS-induced colitis (Cao and Colonna, 2024). The divergent outcomes observed in our study

and those of Cao and Colonna may be attributed to Xbp1-independent roles of IRE1α, such as regulated IRE1α-dependent decay (RIDD) of mRNA, which modulates RIG-I, NF-κB, and interferon pathways in inflammation, as well as promotes apoptosis independent of Xbp1 (Cross et al., 2012; Han et al., 2009; Hollien et al., 2009; Hollien and Weissman, 2006; Hur et al., 2012; Kimmig et al., 2012; Oikawa et al., 2010; Upton et al., 2012). Furthermore, IRE1α activation can also initiate TRAF2 signaling beyond *Xbp1* mRNA splicing and RIDD (Nishitoh et al., 2002; Urano et al., 2000). Given these complexities, targeting Xbp1 specifically, rather than upstream IRE1α, may offer a more precise therapeutic approach for colitis.

ILC3-derived IL-22 plays a key role in counteracting colitis (Cao et al., 2024; Mielke et al., 2013; Wang et al., 2021). In addition to IL-22, ILC3s also produce heparin-binding epidermal growth factor–like growth factor (HB-EGF), which is involved in epithelial protection (Zhou et al., 2022). In our scRNA-seq analysis of colonic tissues from patients with UC, we noticed that *HBEGF* expression was markedly reduced in the ILC2/3 population compared with healthy individuals (Fig. 1 B). Similarly, in a DSS-induced colitis mouse model, we observed downregulation of *Hbegf* expression in colonic ILC3s compared with control mice (Fig. S1 J). These findings suggest that reduced HB-EGF expression in ILC3s, along with impaired ILC2 function, may contribute to disease progression in colitis.

Upon activation, the UPR mediated by IRE1α-Xbp1 signaling is highly mobilized in immune cells, particularly during periods of excessive protein synthesis. Environmental factors also play a role in promoting *Xbp1* mRNA splicing across different immune subsets. For example, TLR2 and TLR4 ligands activate the IRE1α-Xbp1 axis in macrophages (Martinon et al., 2010), ovarian cancer ascites upregulates Xbp1s in T cells (Song et al., 2018), and exposure to high mobility group box 1 induces *Xbp1* splicing in monocyte-derived dendritic cells (Zhu et al., 2012). Our study demonstrated that IL-25 triggered IRE1α phosphorylation and subsequent *Xbp1* mRNA splicing via the p38 pathway, resembling the p38-dependent *Xbp1* splicing enhanced by virulence factors from *Pseudomonas aeruginosa* (Zhou et al., 2021). However, although IL-33 is known to activate p38 MAPK, its treatment of ILC2s only marginally increased *Xbp1* mRNA splicing (Fig. 3, B–D), suggesting that other pathways activated by IL-33 may also modulate IRE1α-Xbp1 signaling in ILC2s.

The suppressive role of IFN-γ in ILC2 activation, proliferation, and function has been well established (Cautivo et al., 2022; Duerr et al., 2016; Kudo et al., 2016; Molofsky et al., 2015; Moro et al., 2016). Specifically, IFN-γ inhibits ILC2 responses to stimuli like IL-33 and TSLP (Cautivo et al., 2022; Kudo et al., 2016; Molofsky et al., 2015), and can directly induce ILC2 apoptosis (Cautivo et al., 2022). This may explain the impaired function of ILC2s in the inflammatory milieu of colitis. Our findings further suggest that IFN-γ suppresses ILC2 function by inhibiting the p38-mediated IRE1α-Xbp1 signaling axis, providing new insights into its role in the pathogenesis of IBD.

While Xbp1s is known to regulate cholesterol and lipid metabolism, our CUT&Tag-seq analysis revealed its enrichment at loci of genes involved in these pathways (Table S5). However, our data suggest that Xbp1s impacts ILC2 function independently of cholesterol, lipid, or glucose metabolism (Fig. S5, O and P; and Table S6). Instead, Xbp1s regulates ILC2s through modulation of DHFR expression to sustain folate-mediated 1C metabolism. Importantly, we identified cAMP, a metabolic product of 1C metabolism, as the critical downstream mediator through which Xbp1s governs colonic ILC2 function. This highlights a cell type–specific metabolic program orchestrated by Xbp1s that influences various cellular functions, including those crucial for gut repair.

Notably, clinical studies have linked UC with folate deficiency (Pan et al., 2017), and the reduction of Xbp1s-regulated DHFR in colitis further supports this defect in folate metabolism. In light of the pivotal role of 1C metabolism in cellular processes, several drugs targeting this pathway, such as MTX (a DHFR inhibitor), are widely used in cancer therapy (Ren et al., 2024). However, MTX can cause adverse gastrointestinal effects, including nausea, vomiting, diarrhea, and mucosal ulcers (Solomon et al., 2020). Our findings suggest that MTX impairs the pro-repair function of intestinal ILC2s (Fig. S5, F–H; and Fig. 5, I, K, and L), offering a potential explanation for the gastrointestinal side effects. Given the significant inhibition of DHFR by MTX in gut ILC2s, supplementation with folate may not sufficiently alleviate these side effects. Instead, supplementation of the 1C metabolite AMP emerges as a promising strategy to restore ILC2 function in the gut, potentially alleviating the intestinal discomfort caused by MTX.

Materials and methods

Mice

Xbp1$^{f/f}$ mice were kindly gifted by Dr. Laurie H. Glimcher (Harvard University, Cambridge, MA, USA). *Il5*$^{RFP\text{-}Cre}$ mice (Cat#: R5/+), *Rorc*-cre mice (Cat#: 022791), and CD45.1/CD45.1 mice (Cat#: 002014) were purchased from Jackson Laboratories. *Rag2*$^{-/-}$*Il2rg*$^{-/-}$ mice (Cat#: 4111) were purchased from Taconic Biosciences. C57BL/6 mice (Cat#: N000013) were purchased from GemPharmatech Co. Ltd. All mice were housed in specific-pathogen-free conditions with *ad libitum* food and water and a light/dark cycle of 12 h. 6- to 14-wk-old male or female mice were used for the experiments. All animal experiments were approved by the Ethics Committee of Shandong University (ECSBMSSDU2020-2-057).

Clinical sample acquisition

Human blood samples and colonic mucosal biopsies were obtained at Qilu Hospital of Shandong University, and the First Affiliated Hospital of Shandong First Medical University (Shandong Provincial Qianfoshan Hospital). The human blood samples were obtained from 10 healthy donors. The human colonic mucosal biopsy samples were obtained from 64 healthy donors and 27 patients with UC. Exclusion criteria of healthy donors were as follows: had polyps >1.0 cm; had intestinal inflammation; combined with malignant tumor. The diagnosis of patients with UC was based on well-established clinical, endoscopic, and histopathological criteria by experienced physicians. Exclusion criteria of patients with UC were as follows: had history of immunosuppressive or hormone therapy; combined with

Crohn's disease, malignant tumor, severe infection. The demographic information of healthy donors and patients with UC is listed in Table S2. The experimental protocols were performed according to the guidelines approved by the Ethics Committee of Shandong University (ECSBMSSDU2020-1-035).

DSS-induced colitis model

Colitis model was induced in mice via administration of 3% (wt/vol) DSS (160110; MP Biomedicals) in the drinking water for 6 days. Mice were monitored daily for weight loss, stool consistency, and hematochezia. DAI was used to evaluate the grade and extent of intestinal inflammation according to the data of weight loss (0–4), stool consistency (0–4), and rectal bleeding (0–4). DAI is calculated as the sum of the three-phase total scores divided by 3 (Kihara et al., 2003). Colon length was measured. The mid-colon tissue was collected and fixed in 4% paraformaldehyde (BL539A; Biosharp), dehydrated, embedded in paraffin, sectioned at 4 µm, and stained with hematoxylin and eosin. For pathological assessment, histology scores were blindly analyzed by a trained gastrointestinal pathologist according to the tissue inflammation (0–5), crypt damage (0–4), ulceration (0–3), and edema (0–1) (Stillie and Stadnyk, 2009).

scRNA-seq and analysis

Mid-colon tissues were obtained from DSS-treated mice. The tissues were transferred into a culture dish containing calcium- and magnesium-free 1× PBS and cut into 0.5-mm pieces on ice. After washing with 1× PBS, the tissues were dissociated into single cells using a dissociation solution (0.35% collagenase IV, 2 mg/ml papain, 120 U/ml DNase I) in 37°C water bath with shaking for 20 min at 100 rpm. Digestion was terminated with 1× PBS containing 10% FBS, then pipetted 5–10 times with a Pasteur pipette. The resulting cell suspension was filtered through a 70- to 30-µm stacked cell strainer and centrifuged at 300 *g* for 5 min at 4°C. The cell pellet was resuspended in 100 µl 1× PBS containing 0.04% BSA and 1 ml 1× red blood cell lysis buffer (130-094-183; Miltenyi Biotec) and incubated to lyse remaining red blood cells. After centrifugation, dead cells in the pellet were removed using Dead Cell Removal Kit (130-090-101; Miltenyi Biotec). Then, the suspension was resuspended in 1× PBS containing 0.04% BSA and centrifuged at 300 *g* for 3 min at 4°C (repeat twice). After resuspending the cell pellet in 50 µl 1× PBS containing 0.04% BSA, cell viability was confirmed by trypan blue exclusion to ensure a viability of >85%. Single-cell suspensions were counted using Countess II Automated Cell Counter, and the concentration was adjusted to 700–1,200 cells/µl.

Single-cell suspensions were loaded to 10× Chromium to capture 5,000 single cells according to the manufacturer's instructions of 10× Genomics Chromium Single-Cell 3′ Kit. The following cDNA amplification and library construction steps were performed according to the standard protocol. Libraries were sequenced on an Illumina NovaSeq 6000 sequencing system (paired-end multiplexing run, 150 bp) by LC-Bio Technology Co. Ltd. at a minimum depth of 20,000 reads per cell.

Raw fastq files were mapped to the mouse transcriptome ("refdata-gex-mm10-2020") using Cell Ranger (10× Genomics, version 8.0.0) provided by 10× Genomics to generate the unique molecular identifier matrix. Single-cell analysis was performed using Seurat (version 4.1.0) (Hao et al., 2021). Specifically, cells with <200 detected genes, >6,000 detected genes, and/or mitochondrial read fraction >10% were filtered out. After filtering, 52,228 cells were carried through for subsequent analyses. We applied Seurat's NormalizeData function to normalize read counts. Principal component analysis (PCA) was performed on highly variable genes, and the first 30 PCA components were used for downstream analyses. We applied the Harmony algorithm (Korsunsky et al., 2019) to correct the batch effects from different experiments. We performed tSNE dimensional reduction using 30 principal components. Cells were clustered using Seurat's FindClusters function with a resolution of 0.6. We annotated each cell cluster according to canonical cell markers, and identified the major cell types by co-expression of known markers of different cell types.

To compare the profile of immune cell populations in our study, we subset the *Ptprc*$^{+}$ cell clusters and performed PCA, batch effect correction, unsupervised cell clustering, and dimensionality reduction as described above. Contaminants were identified based on gene expression signatures determined using the function FindAllMarkers with a minimum $\log_2$ fold change threshold of 0.25 and the Wilcoxon rank sum test. Based on the DEG analysis, epithelial cell clusters marked by *Epcam* were removed, and each immune cell cluster was annotated according to canonical cell markers to identify the intestinal immune cell types. scRNA-seq data have been deposited in the Gene Expression Omnibus (GEO) under the accession number GSE268235 and are publicly available upon online publication.

RNA extraction and qRT-PCR

Total RNA was extracted using TRIzol (R401-01; Vazyme), and cDNA was generated from each RNA sample using the HiScript III Reverse Transcriptase SuperMix kit (R323-01; Vazyme) according to the manufacturer's protocol. Quantitative PCR was run on a Real Time PCR System (StepOne; Applied Biosystems) using SYBR Green Master Mix (Q711-02; Vazyme). The mRNA levels of specific genes were normalized against *Gapdh* levels. The data were analyzed using the $2^{-\Delta\Delta Ct}$ method. The primer pairs used for target genes are listed in Table S7.

Isolation of intestinal LPLs

The isolation of mouse intestinal LPLs was conducted as previously described (Qiu et al., 2012). Briefly, the large intestines were separated, and fat tissues were removed. Intestines were cut open longitudinally and washed in PBS, and were cut into 5-mm pieces. The tissues were incubated in PBS containing 10 mM EDTA (E1170; Solarbio) and 20 mM HEPES (H8090; Solarbio) with shaking at 200 rpm at 37°C for 30 min. Then, the tissues were digested in RPMI 1640 medium (CM10040; Macgene) containing 5% FBS, 1% penicillin–streptomycin (CC004; Macgene), DNase I (150 µg/ml, DN25; Sigma-Aldrich), and collagenase VIII (150 U/ml, C2139; Sigma-Aldrich) at 37°C in 5% CO_2 incubator for 1.5 h. The digested tissues were shaken and dissociated into single cells, and then filtered through a 100-µm cell strainer. After gradient centrifugation at 2,500 rpm for 15 min at

room temperature, mononuclear cells were harvested from the middle layer of the 40% and 80% Percoll (17089109; Cytiva) purification system.

For the isolation of human LPMNCs, the mucosal tissues were washed twice in PBS, and then incubated in PBS containing 10 mM EDTA and 5% FBS at 37°C with shaking at 220 rpm for 20 min. After washing once in RPMI 1640 medium, the mucosal tissues were digested for 30 min in RPMI 1640 medium containing 5% FBS, 1% penicillin-streptomycin, DNase I (150 μg/ml), and collagenase IV (5 mg/ml, C5138; Sigma-Aldrich) with shaking at 80 rpm at 37°C. The digested tissues were shaken and dissociated into single cells, and filtered through a 100-μm cell strainer. After centrifugation, the mononuclear cell pellets were harvested.

Flow cytometry and cell sorting

The live and dead cells were discriminated by the Zombie Aqua Fixable Viability Kit (423102; BioLegend) in PBS. Anti-mouse CD16/32 antibody was used to block the non-specific binding to Fc receptors before surface staining. Surface antibody staining was performed in PBS containing 2 mM EDTA and 2% FBS for 25 min at 4°C. For intracellular staining, cells were fixed and permeabilized with fixation/permeabilization buffer (eBioscience) at 4°C overnight. After fixation, the cells were washed and incubated with the indicated antibodies in 1× permeabilization buffer (eBioscience) at 4°C for 2 h. For cytokine production, cells were stimulated by 50 ng/ml PMA (1652981; BioGems) and 500 ng/ml ionomycin (5608212; BioGems) for 4 h, and 2 μg/ml brefeldin A (2031560; BioGems) was added for the last 2 h before cells were harvested. Lineage-positive cells were excluded from the analysis of ILCs by staining for the mix (Lin) that contained CD3, CD5, CD19, B220, Ly6G, CD11b, CD11c, Ter119, FcεRIα, and CD16/32. Flow cytometry was performed using the Gallios Flow Cytometer (Beckman Coulter) and analyzed with FlowJo software (TreeStar). Cell sorting was performed on MoFlo Astrios EQs (Beckman Coulter) or BD FACSMelody (BD Bioscience). ILC2s were sorted as $CD45.2^+Lin^-CD127^+KLRG1^+$ population from mouse large intestinal LPLs. A list of flow cytometry antibodies used is available in Table S8.

Cell culture

Mouse intestinal LPLs were cultured in IMDM (CM10016; Macgene) supplemented with 5% FBS (F8687; Sigma-Aldrich) for 4 h. Sorted large intestinal ILC2s were cultured in IMDM supplemented with 10% FBS, rmIL-2 (10 ng/ml, 212-12; PeproTech), rmIL-7 (10 ng/ml, 577802; BioLegend), rmIL-25 (10 ng/ml, 210-17E; PeproTech) for indicated times. Human LPMNCs were cultured in RPMI 1640 medium (CM10040; Macgene) supplemented with 10% FBS for indicated times. Human ILC2s were cultured in IMDM supplemented with 10% FBS, hIL-2 (20 ng/ml, 200-02; PeproTech), hIL-7 (20 ng/ml, 200-07; PeproTech), hIL-25 (20 ng/ml, 200-24; PeproTech), and hIL-33 (20 ng/ml, 200-33; PeproTech) for indicated times. The complete medium contains both 1% penicillin–streptomycin (CC004; Macgene) and 0.1% gentamycin (MA005; Macgene). All cells are cultured in 5% CO_2 incubator at 37°C.

RNA-seq analysis

Total RNA was extracted using TRIzol reagent (R401-01; Vazyme). The RNA amount and purity was quantified using NanoDrop ND-1000 (NanoDrop). The RNA integrity was assessed using the Bioanalyzer 2100 (Agilent), and high-quality RNA samples with RIN number >7.0 were used for library construction. For bulk RNA-seq, Dynabeads Oligo (dT) (25-61005; Thermo Fisher Scientific) were used for specific capture of mRNA through two rounds of purification. The captured mRNA was fragmented into small pieces using NEBNext Magnesium RNA Fragmentation Module (E6150; NEB) at 94°C for 5–7 min. The fragmented RNA was reverse-transcribed into cDNA using SuperScript II Reverse Transcriptase (1896649; Invitrogen), which was next used to synthesis U-labeled second-stranded DNAs with DNA polymerase I (*E. coli*) (M0209; NEB), RNase H (M0297; NEB), and dUTP solution (R0133; Thermo Fisher Scientific). An A-base was then added to both ends to enable ligation with adapters that have a T-base at the end. The fragments were further size-selected and purified using AMPure XP beads. After the heat-labile UDG enzyme (M0280; NEB) treatment of the second-stranded DNAs, the ligated products are amplified with PCR by the following conditions: initial denaturation at 95°C for 3 min; 8 cycles of denaturation at 98°C for 15 s, annealing at 60°C for 15 s, and extension at 72°C for 30 s; and then extension at 72°C for 5 min to form a library with fragment size of 300 ± 50 bp. Finally, we performed the 2 × 150 bp paired-end sequencing (PE150) on the Illumina NovaSeq 6000 (LC-Bio Technology CO., Ltd.) following the vendor's recommended protocol. Bulk RNA-seq data have been deposited in the GEO under the accession number GSE268233 and are publicly available upon online publication.

For SMART-seq, full-length cDNA was generated using SMART-Seq HT Kit (634437; Takara); paired-end DNA libraries was generated and indexed using Nextera XT Library Prep Kit (15032350; Illumina) and then Nextera XT Index Kit (15052163; Illumina). Barcoded samples were pooled and sequenced-run with Illumina NovaSeq 6000 sequence platform, generating 2 × 150 bp paired-end reads. The reads were further filtered by Cutadapt (version: cutadapt-4.7). Filtered reads were mapped to the reference genome mm10 assembly of the *Mus musculus* genome (National Center for Biotechnology Information) using hisat2 (version 2.2.1). Significantly changed genes were identified by DESeq2. SMART-seq data have been deposited in the GEO under the accession number GSE303533 and are publicly available upon online publication.

In vivo treatment of mice

For AMP (HY-W011012; MedChemExpress) treatment *in vivo*, mice were gavaged with AMP at a dose of 800 mg/kg or water for 5 consecutive days and sacrificed for analysis on day 6.

For toyocamycin (HY-103248; MedChemExpress) treatment *in vivo*, mice were treated every other day for four times with 100 μl vehicle (10% DMSO, 40% PEG400, and 5% Tween-80 in distilled water) or toyocamycin at a dose of 0.7 mg/kg body weight by intraperitoneal injection. Mice were sacrificed and collected in the large intestine for analysis of ILC2 effector function on day 7.

For rmIL-25 and anti-IFN-γ treatment experiment *in vivo*, rmIL-25 (RP01799; ABclonal) was given as 0.4 μg in 200 μl PBS intraperitoneally (i.p.) every day for five doses; while the mice were injected i.p. with 1 mg anti-IFN-γ (A2105; Selleck) on days −1, 2, and 5, the mice were sacrificed for analysis on day 6. PBS and corresponding isotypes IgG (A2119; Selleck) were used as a vehicle control.

ELISA

The concentrations of IL-25 and IFN-γ in mouse colon tissues and blood were determined by ELISA. The colon tissues were collected and placed into 1.5-ml Eppendorf tubes, followed by homogenization in ice-cold PBS. After centrifugation at 12,000 *g* for 10 min at 4°C, the supernatants were collected for subsequent analysis. Protein concentrations in the supernatant were measured using BCA Protein Assay Kit (P0012; Beyotime). The concentrations of IL-25 and IFN-γ were measured using Mouse IL-25 ELISA Kit (EK2179; Multi Sciences) and Mouse IFN-γ ELISA Kit (EK280; Multi Sciences), respectively, following the manufacturer's instructions. The collected mouse blood was allowed to clot at room temperature, and then centrifuged at 7,000 rpm for 10 min to obtain serum, which was used for IFN-γ detection using Mouse IFN-γ ELISA Kit (EK280; Multi Sciences).

HPLC-MS/MS analysis

The cellular AMP, GMP, SAM, and dTMP were determined using a HPLC-MS/MS system with an ADME column (100 × 2.1 mm). ILC2s were extracted in 600 μl acetonitrile, followed by additions of IS working solution ($^{13}C_{10}{}^{15}N_5$-GMP, 10 μg/ml, 10 μl) and methanol–water (5:95, vol/vol, 10 μl). The mixture was extracted by shocking for 3 min and then centrifuged at 12,000 *g* for 20 min at 4°C. The supernatants were transferred to another 1.5-ml Eppendorf tube and evaporated to dryness at 30°C by a vacuum extractor. The residue was reconstituted in 150 μl of initial mobile phase. For analysis of AMP, GMP, and dTMP, negative ion mode was used. The positive ion mode was used for analysis of SAM. The mobile phase consisted of 5 μM DMP in 5 mM NH_4FA (A) and acetonitrile–water (95:5, vol/vol) (B). The gradient elution program was as follows: 0–3 min, 98% A; 3–5 min, 98–95% A; 5–7 min, 95–10% A; 7–11 min, 10% A; 11–15 min, 98% A. Respective standards were used to generate standard calibration curves. Samples were analyzed on a Qtrap 5500 (AB Sciex) system.

1C metabolomics assay

ILC2s were extracted in 100 μl acetonitrile, followed by additions of IS working solution. The mixture was extracted by shocking for 3 min and then centrifuged at 18,000 *g* for 20 min at 4°C. For folic acid, folinic acid, and 5-MTHF measurement, 20 μl supernatants were added with 75 μl vitamin C, then centrifuged at 18,000 *g* for 20 min at 4°C, and the supernatants were used for analysis. The samples were analyzed using an ACQUITY UPLC BEH C18 analytical column (100 × 2.1 mm). The mobile phase consisted of formate–water (0.1:100, vol/vol) (A) and formate–acetonitrile (0.1:100, vol/vol) (B). The gradient elution program was as follows: 0–2 min, 2–5% B; 2–3 min, 5–90% B; 3–3.8 min, 90% B; 3.8–4 min, 90–2% B; 4–5 min, 2% B.

For methionine, SAM, SAH, homocysteine, cystathionine, cystine, cysteine, serine, and glycine measurement, 20 μl supernatants were added with 70 μl boric acid buffer and 20 μl 6-aminoquinolyl-N-hydroxysuccinimidyl carbamate, and then incubated at 55°C for 10 min; afterward, 900 μl of ddH_2O was added to the samples and vortexed, and 100 μl supernatants were used for analysis. The mobile phase consisted of formate–water (0.1:100, vol/vol) (A) and formate–acetonitrile (0.1:100, vol/vol) (B). The gradient elution program was as follows: 0–0.5 min, 4% B; 0.5–2.5 min, 0.5–2.5% B; 2.5–5 min, 10–28% B; 5–6 min, 28–95% B; 6–7 min, 95% B; 7–7.7 min, 95–4% B; 7.7–9 min, 4% B.

Respective standards were used to generate standard calibration curves. Samples were analyzed on an ACQUITY UPLC-Xevo TQ-S (Waters Crop.) system by Metabo-Profile Biotechnology. The metabolite levels were normalized by the total cell amount per sample.

Adoptive transfer of ILC2s

For *in vivo* competitive transfer experiment, large intestinal ILC2s from *Xbp1*$^{+/+}$*Il5*$^{\text{RFP-Cre}}$ (CD45.1/CD45.1) and *Xbp1*$^{f/f}$*Il5*$^{\text{RFP-Cre}}$ (CD45.2/CD45.2) were purified by flow cytometry and collected in complete IMDM. Sorted ILC2s were quantified and mixed at 1:1 ratio in sterile 1× PBS, and 2 × 10^5 ILC2s in total were intravenously transferred into *Rag2*$^{-/-}$*Il2rg*$^{-/-}$ recipient mice. Recipient mice were euthanized for analysis after 2 wk.

For adoptive transfer of ILC2s under colitis, large intestinal ILC2s from *Xbp1*$^{f/f}$*Il5*$^{\text{RFP-Cre}}$ or littermate *Xbp1*$^{+/+}$*Il5*$^{\text{RFP-Cre}}$ mice were cultured in complete IMDM containing IL-2, IL-7, and IL-25 (10 ng/ml each) for 5 days. 1 × 10^7 ILC2s were transferred into *Rag2*$^{-/-}$*Il2rg*$^{-/-}$ mice at day −2, day 0, day 2, and day 4 and fed with 3% DSS for 6 days to an induced colitis model. PBS was used as a vehicle control. The disease severity was assessed after the induction of colitis.

Western blotting

Total protein from ILC2s was extracted using radioimmunoprecipitation assay lysis buffer (G2002; Servicebio) freshly supplemented with 1× protein phosphatase inhibitor (P1260; Solarbio), 1× protease inhibitor cocktail (HY-K0010; MedChemExpress), and PMSF (1 mM, P0100; Solarbio). 1 × 10^5 ILC2s were used for the western blotting experiments, and the total protein was loaded and separated on 10% SDS-PAGE gel and transferred onto polyvinylidene fluoride (PVDF) membranes (Millipore). The membranes were blocked with 5% skim milk (A600669; Sangon Biotech) in tris buffered saline with Tween-20 (TBST) for 1 h at room temperature and incubated with indicated primary antibodies overnight at 4°C. After washing three times for 5 min with TBST, membranes were incubated with corresponding secondary HRP-conjugated antibody diluted in 5% skim milk for 1 h at room temperature. Membranes were washed three times for 5 min with TBST, and then detected using the enhanced chemiluminescence reagents (BL520B; Biosharp) and captured by a chemiluminescence imaging system (Tanon). Antibodies used for western blotting included phospho-IRE1α (Ab124945; Abcam), Xbp1s (40435; Cell Signaling Technology), DHFR (15194-1-AP; Proteintech), Phospho-p38

(4511; Cell Signaling Technology), β-actin (66009-1-Ig; Proteintech), goat anti-rabbit IgG-HRP–conjugated antibody (SA00001-2; Proteintech), goat anti-mouse IgG-HRP–conjugated antibody (SA00001-1; Proteintech).

CUT&Tag and data processing

The CUT&Tag assay was conducted using Hyperactive Universal CUT&Tag Assay Kit for Illumina Pro (TD904; Vazyme). Two biological replicates were performed for each of the negative control (IgG) and the experimental group (Xbp1s). Briefly, 1.5 × 10^5 ILC2s were collected and washed with 500 µl wash buffer before they were bound to concanavalin A–coated magnetic beads for 15 min at room temperature. Subsequently, IgG antibody (A7016; Beyotime)-beads or Xbp1s antibody (40435; Cell Signaling Technology)-beads were incubated at 4°C overnight. Secondary antibody was added and incubated for 1 h at room temperature the next day. Then, cells were incubated with 0.04 µM pA/G-Tnp Pro for 1 h at room temperature. Next, sample was tagmentated in tagmentation buffer at 37°C for 1 h. The DNA was extracted and dissolved in 20 µl nuclease-free water according to the manufacturer's instructions. Libraries were paired-end–sequenced (150 bp × 2) with a NovaSeq X Plus (Illumina).

The clean reads were aligned to mouse reference genome mm10 using bowtie2 (version 2.5.1). For advanced filtering, SAMtools (version 1.18) were used to remove blacklist-region reads. Then, the clean BAM files were used to generate normalized bigwig files and heatmap over transcription units with deepTools (version 3.5.5). Peaks were then called using MACS2 (version 2.2.9.1). Integrated Genomics Viewer (version 2.14.1) was used to assess the signals of the clean BAM files and normalized bigwig files. Gene component and percent distribution analysis of Xbp1s binding sites was performed using ChIPseeker (version 1.36.0). KEGG analysis of genes related to Xbp1s-binding peaks was done using clusterProfiler (version 4.8.3). CUT&Tag-seq data have been deposited in the GEO under the accession number GSE268234 and are publicly available upon online publication.

Retroviral transduction of ILC2s

The cDNAs of target genes were cloned into MSCV–IRES–Thy1.1 retroviral vectors. HEK293T cells were transfected with retroviral plasmids and the packaging plasmid 10A1 using polyethylenimine. The viral supernatant was collected 48 h after transfection. Sorted large intestinal ILC2s were cultured in a 24-well plate with the complete IMDM. After 5 days of culture, 0.45 µm filtered retrovirus-containing supernatants supplemented with polybrene (8 µg/ml, C0351; Beyotime) were added to the cells followed by centrifugation at 2,500 rpm for 2 h at 30°C. The cells were cultured for another 4 days before collection for analysis.

Dual luciferase reporter assay

Dhfr firefly luciferase reporter plasmid was generated by inserting the −1,000 to +532 bp of the mouse *Dhfr* gene between the KpnI and XhoI sites of the pGL3-Basic vector. Mouse *Xbp1s* expression plasmid was purchased from Youbio (G138942). HEK293T cells were cultured in 24-well plate and transfected with expression plasmids (300 ng of empty plasmid pcDNA3.1 or *Xbp1s* expression plasmid), luciferase reporter plasmids (300 ng of wild-type or mutant *Dhfr*-pGL3 reporter plasmid), and 3 ng of Renilla luciferase reporter plasmid using jetPRIME Transfection Reagent (101000046; Polyplus). After 24-h transfection, HEK293T cells were washed once with PBS gently. The activities of firefly and Renilla luciferases were measured using the Dual Luciferase Reporter Gene Assay Kit (RG027; Beyotime) following the manufacturer's protocol, and the luminescence was read on a microplate reader (Centro LB 960; Berthold Technologies). Firefly luciferase activity was normalized to Renilla luciferase activity.

Immunohistochemistry staining

For tuft cell staining, the mid-colonic tissues were flushed with PBS and fixed in 4% paraformaldehyde (BL539A; Biosharp) for 24 h at room temperature. Tissues were then dehydrated, embedded in paraffin, and sliced into 4 µm. The tissue slides were deparaffinized, rehydrated, and boiled in 10 mM citrate for 10 min. Slides were allowed to cool to room temperature, washed with PBS, and then incubated with endogenous peroxidase blockers (PV-9000; ZSGB-BIO). After blocked with goat serum working solution (ZLI-9056; ZSGB-BIO), the slides were then incubated with the primary antibody anti-DCLK1 (1:100, Ab109029; Abcam) overnight at 4°C, followed by incubation with HRP-linked secondary antibody for 2 h at room temperature. Slides were washed with PBS and then developed with the DAB substrate kit (ZLI-9018; ZSGB-BIO) and counterstained with hematoxylin. The sections were scanned and stitched by Olympus VS120 slide scanner.

Statistical analysis

Statistical analysis was performed using GraphPad Prism 8 (GraphPad Software). Student's unpaired *t* test was employed for comparisons between two groups, unless otherwise indicated. Differences were considered significant at P values <0.05 (*P < 0.05, **P < 0.01, ***P < 0.001; ns, not significant). Data are displayed as the mean ± SD.

Online supplemental material

Fig. S1 provides additional data relevant to Fig. 1, including scRNA-seq analysis of human colonic immune cells, flow cytometry gating strategy for identifying human colonic ILCs, and analysis of impaired function in colonic ILC2s during colitis. Fig. S2 illustrates that Xbp1s regulates gut ILC2s in a cell-intrinsic manner. Fig. S3 shows that IL-25 sustains gut ILC2 function and the production of IL-25 in tuft cells decreased during colitis. Fig. S4 shows that IFN-γ significantly restrains intestinal ILC2 function, and includes analysis related to CUT&Tag-seq. Fig. S5 shows that Xbp1s targets DHFR to regulate folate-mediated 1C metabolism in gut ILC2s, and illustrates that the regulation of ILC2s by Xbp1s is independent of cholesterol and palmitic acid. Table S1 lists the marker genes defining human immune cell subsets. Table S2 lists the demographic information of UC participants and healthy donors. Table S3 lists the marker genes defining mouse colonic $CD45^+$ immune cell subsets. Table S4 lists the marker genes defining all colonic cell types in mouse. Table

S5 lists the Xbp1s binding genes in large intestinal ILC2s analyzed by CUT&Tag-seq. Table S6 lists the overlapping gene analysis between Xbp1s-binding genes with DEGs in toyocamycin-treated ILC2s. Table S7 lists the sequences of primers used for qRT-PCR. Table S8 lists the antibodies used for flow cytometry, and reagents and recombinant proteins used for ILC2 treatment.

Data availability

The scRNA-seq data presented in Figs. 1, S1, and S3 were generated in this study and have been deposited in the GEO under the accession code GSE268235. The control group was generated from untreated mice by public data GSE210415 (Zheng et al., 2024). The bulk RNA-seq data presented in Fig. 1 were generated in this study and have been deposited in the GEO under the accession code GSE268233. SMART-seq data presented in Figs. S1 and S2 were generated in this study and are available from GEO under the accession code GSE303533. CUT&Tag-seq data presented in Figs. 5 and S4 were generated in this study and have been deposited in the GEO under the accession code GSE268234. The scRNA-seq data presented in Fig. 1 are available from the public dataset GSE125527 (Boland et al., 2020). The bulk RNA--seq data presented in Fig. 3 were generated from GSE210405 (Zheng et al., 2024). Source data are provided with this paper. All other data supporting the findings of this study are available from the corresponding author on reasonable request.

Acknowledgments

We thank the entire Li lab for help and suggestions to this study. We thank the Translational Medicine Core Facility and Center of Drug Analysis and Test of Shandong University for consultation and instrument availability that supported this work.

This work was financially supported by National Key R&D Program of China (2020YFA0804400), National Natural Science Foundation of China (82071854, 82270621, and 82321002), Taishan Scholars Program of Shandong Province, and Natural Science Foundation of Shandong Province (ZR2023QH269).

Author contributions: Yanyan Cui: conceptualization, formal analysis, investigation, methodology, visualization, and writing—original draft, review, and editing. Zixiao Zhao: conceptualization, data curation, formal analysis, funding acquisition, investigation, methodology, project administration, resources, validation, visualization, and writing—original draft, review, and editing. Jing Shen: data curation, methodology, and writing—original draft. Yatai Chen: data curation and formal analysis. Qiuheng Tian: investigation and project administration. Yang Liu: investigation. Yunjiao Zhai: methodology. Bowen Xu: methodology. Jiajie Hou: resources. Chunyang Li: resources. Yanbo Yu: investigation. Xiaohuan Guo: resources. Ju Qiu: resources. Detian Yuan: conceptualization and writing—original draft, review, and editing. Shiyang Li: conceptualization, funding acquisition, project administration, supervision, and writing—original draft, review, and editing.

Disclosures: The authors declare no competing interests exist.

Submitted: 26 February 2025
Revised: 7 August 2025
Accepted: 23 September 2025

References

Abt, M.C., B.B. Lewis, S. Caballero, H. Xiong, R.A. Carter, B. Sušac, L. Ling, I. Leiner, and E.G. Pamer. 2015. Innate immune defenses mediated by two ILC subsets are critical for protection against acute Clostridium difficile infection. *Cell Host Microbe*. 18:27–37. https://doi.org/10.1016/j.chom.2015.06.011

Ali, M.M.U., T. Bagratuni, E.L. Davenport, P.R. Nowak, M.C. Silva-Santisteban, A. Hardcastle, C. McAndrews, M.G. Rowlands, G.J. Morgan, W. Aherne, et al. 2011. Structure of the Ire1 autophosphorylation complex and implications for the unfolded protein response. *EMBO J.* 30:894–905. https://doi.org/10.1038/emboj.2011.18

Boland, B.S., Z. He, M.S. Tsai, J.G. Olvera, K.D. Omilusik, H.G. Duong, E.S. Kim, A.E. Limary, W. Jin, J.J. Milner, et al. 2020. Heterogeneity and clonal relationships of adaptive immune cells in ulcerative colitis revealed by single-cell analyses. *Sci. Immunol.* 5:eabb4432. https://doi.org/10.1126/sciimmunol.abb4432

Branche, E., Y.-T. Wang, K.M. Viramontes, J.M.V. Cuevas, J. Xie, F. Ana-Sosa-Batiz, N. Shafee, S.H. Duttke, R.E. McMillan, A.E. Clark, et al. 2022. SREBP2-dependent lipid gene transcription enhances the infection of human dendritic cells by Zika virus. *Nat. Commun.* 13:5341. https://doi.org/10.1038/s41467-022-33041-1

Cao, S., and M. Colonna. 2024. IRE1A-XBP1 controls group 2 innate lymphoid cells in intestinal inflammation and fibrosis. *Gastroenterology*. 166:S98.

Cao, S., J.L. Fachi, K. Ma, A.U. Antonova, Q. Wang, Z. Cai, R.J. Kaufman, M.A. Ciorba, P. Deepak, and M. Colonna. 2024. The IRE1 α/XBP1 pathway sustains cytokine responses of group 3 innate lymphoid cells in inflammatory bowel disease. *J. Clin. Invest.* 134:e174198. https://doi.org/10.1172/jci174198

Casali, C., R. Malvicini, L. Erjavec, L. Parra, A. Artuch, and M.C. Fernández Tome. 2020. X-Box binding protein 1 (XBP1): A key protein for renal osmotic adaptation. Its role in lipogenic program regulation. *Biochim. Biophys. Acta Mol. Cell Biol. Lipids*. 1865:158616. https://doi.org/10.1016/j.bbalip.2020.158616

Cautivo, K.M., P.R. Matatia, C.O. Lizama, N.M. Mroz, M.W. Dahlgren, X. Yu, J. Sbierski-Kind, M.T. Taruselli, J.F. Brooks, A. Wade-Vallance, et al. 2022. Interferon gamma constrains type 2 lymphocyte niche boundaries during mixed inflammation. *Immunity*. 55:254–271.e7. https://doi.org/10.1016/j.immuni.2021.12.014

Cross, B.C.S., P.J. Bond, P.G. Sadowski, B.K. Jha, J. Zak, J.M. Goodman, R.H. Silverman, T.A. Neubert, I.R. Baxendale, D. Ron, and H.P. Harding. 2012. The molecular basis for selective inhibition of unconventional mRNA splicing by an IRE1-binding small molecule. *Proc. Natl. Acad. Sci. USA*. 109:E869-E878. https://doi.org/10.1073/pnas.1115623109

Cubillos-Ruiz, J.R., P.C. Silberman, M.R. Rutkowski, S. Chopra, A. Perales-Puchalt, M. Song, S. Zhang, S.E. Bettigole, D. Gupta, K. Holcomb, et al. 2015. ER stress sensor XBP1 controls anti-tumor immunity by disrupting dendritic cell homeostasis. *Cell*. 161:1527–1538. https://doi.org/10.1016/j.cell.2015.05.025

Di Conza, G., P.-C. Ho, J.R. Cubillos-Ruiz, and S.C.-C. Huang. 2023. Control of immune cell function by the unfolded protein response. *Nat. Rev. Immunol.* 23:546–562. https://doi.org/10.1038/s41577-023-00838-0

Dong, H., N.M. Adams, Y. Xu, J. Cao, D.S.J. Allan, J.R. Carlyle, X. Chen, J.C. Sun, and L.H. Glimcher. 2019. The IRE1 endoplasmic reticulum stress sensor activates natural killer cell immunity in part by regulating c-Myc. *Nat. Immunol.* 20:865–878. https://doi.org/10.1038/s41590-019-0388-z

Duan, J., J.D. Matute, L.W. Unger, T. Hanley, A. Schnell, X. Lin, N. Krupka, P. Griebel, C. Lambden, B. Sit, et al. 2023. Endoplasmic reticulum stress in the intestinal epithelium initiates purine metabolite synthesis and promotes Th17 cell differentiation in the gut. *Immunity*. 56:1115–1131.e9. https://doi.org/10.1016/j.immuni.2023.02.018

Duerr, C.U., C.D.A. McCarthy, B.C. Mindt, M. Rubio, A.P. Meli, J. Pothlichet, M.M. Eva, J.-F. Gauchat, S.T. Qureshi, B.D. Mazer, et al. 2016. Type I interferon restricts type 2 immunopathology through the regulation of group 2 innate lymphoid cells. *Nat. Immunol.* 17:65–75. https://doi.org/10.1038/ni.3308

Gerlach, K., Y. Hwang, A. Nikolaev, R. Atreya, H. Dornhoff, S. Steiner, H.-A. Lehr, S. Wirtz, M. Vieth, A. Waisinan, et al. 2014. TH9 cells that express the transcription factor PU.1 drive T cell-mediated colitis via IL-9

receptor signaling in intestinal epithelial cells. *Nat. Immunol.* 15: 676–686. https://doi.org/10.1038/ni.2920
Grootjans, J., A. Kaser, R.J. Kaufman, and R.S. Blumberg. 2016. The unfolded protein response in immunity and inflammation. *Nat. Rev. Immunol.* 16: 469–484. https://doi.org/10.1038/nri.2016.62
Guo, C., Z. Chi, D. Jiang, T. Xu, W. Yu, Z. Wang, S. Chen, L. Zhang, Q. Liu, X. Guo, et al. 2018. Cholesterol homeostatic regulator SCAP-SREBP2 integrates NLRP3 inflammasome activation and cholesterol biosynthetic signaling in macrophages. *Immunity*. 49:842–856.e7. https://doi.org/10.1016/j.immuni.2018.08.021
Han, D., A.G. Lerner, L. Vande Walle, J.-P. Upton, W. Xu, A. Hagen, B.J. Backes, S.A. Oakes, and F.R. Papa. 2009. IRE1alpha kinase activation modes control alternate endoribonuclease outputs to determine divergent cell fates. *Cell*. 138:562–575. https://doi.org/10.1016/j.cell.2009.07.017
Hao, Y., S. Hao, E. Andersen-Nissen, Mauck W.M. 3rd, S. Zheng, A. Butler, M.J. Lee, A.J. Wilk, C. Darby, M. Zager, et al. 2021. Integrated analysis of multimodal single-cell data. *Cell*. 184:3573–3587.e29. https://doi.org/10.1016/j.cell.2021.04.048
Hetz, C., K. Zhang, and R.J. Kaufman. 2020. Mechanisms, regulation and functions of the unfolded protein response. *Nat. Rev. Mol. Cell Biol.* 21: 421–438. https://doi.org/10.1038/s41580-020-0250-z
Hollien, J., J.H. Lin, H. Li, N. Stevens, P. Walter, and J.S. Weissman. 2009. Regulated Ire1-dependent decay of messenger RNAs in mammalian cells. *J. Cell Biol.* 186:323–331. https://doi.org/10.1083/jcb.200903014
Hollien, J., and J.S. Weissman. 2006. Decay of endoplasmic reticulum-localized mRNAs during the unfolded protein response. *Science*. 313: 104–107. https://doi.org/10.1126/science.1129631
Hur, K.Y., J.-S. So, V. Ruda, M. Frank-Kamenetsky, K. Fitzgerald, V. Koteliansky, T. Iwawaki, L.H. Glimcher, and A.-H. Lee. 2012. IRE1α activation protects mice against acetaminophen-induced hepatotoxicity. *J. Exp. Med.* 209:307–318. https://doi.org/10.1084/jem.20111298
Iwakoshi, N.N., M. Pypaert, and L.H. Glimcher. 2007. The transcription factor XBP-1 is essential for the development and survival of dendritic cells. *J. Exp. Med.* 204:2267–2275. https://doi.org/10.1084/jem.20070525
Kamimura, D., and M.J. Bevan. 2008. Endoplasmic reticulum stress regulator XBP-1 contributes to effector $CD8^+$ T cell differentiation during acute infection. *J. Immunol.* 181:5433–5441. https://doi.org/10.4049/jimmunol.181.8.5433
Kaser, A., and R.S. Blumberg. 2009. Endoplasmic reticulum stress in the intestinal epithelium and inflammatory bowel disease. *Semin. Immunol.* 21:156–163. https://doi.org/10.1016/j.smim.2009.01.001
Kaser, A., A.-H. Lee, A. Franke, J.N. Glickman, S. Zeissig, H. Tilg, E.E.S. Nieuwenhuis, D.E. Higgins, S. Schreiber, L.H. Glimcher, and R.S. Blumberg. 2008. XBP1 links ER stress to intestinal inflammation and confers genetic risk for human inflammatory bowel disease. *Cell*. 134: 743–756. https://doi.org/10.1016/j.cell.2008.07.021
Kato, A. 2019. Group 2 innate lymphoid cells in airway diseases. *Chest*. 156: 141–149. https://doi.org/10.1016/j.chest.2019.04.101
Kihara, N., S.G. de la Fuente, K. Fujino, T. Takahashi, T.N. Pappas, and C.R. Mantyh. 2003. Vanilloid receptor-1 containing primary sensory neurones mediate dextran sulphate sodium induced colitis in rats. *Gut*. 52: 713–719. https://doi.org/10.1136/gut.52.5.713
Kimmig, P., M. Diaz, J. Zheng, C.C. Williams, A. Lang, T. Aragon, H. Li, and P. Walter. 2012. The unfolded protein response in fission yeast modulates stability of select mRNAs to maintain protein homeostasis. *Elife*. 1: e00048. https://doi.org/10.7554/eLife.00048
Korsunsky, I., N. Millard, J. Fan, K. Slowikowski, F. Zhang, K. Wei, Y. Baglaenko, M. Brenner, P.-R. Loh, and S. Raychaudhuri. 2019. Fast, sensitive and accurate integration of single-cell data with Harmony. *Nat. Methods*. 16:1289–1296. https://doi.org/10.1038/s41592-019-0619-0
Kudo, F., M. Ikutani, Y. Seki, T. Otsubo, Y.I. Kawamura, T. Dohi, K. Oshima, M. Hattori, S. Nakae, K. Takatsu, and S. Takaki. 2016. Interferon-γ constrains cytokine production of group 2 innate lymphoid cells. *Immunology*. 147:21–29. https://doi.org/10.1111/imm.12537
Madison, B.B. 2016. Srebp2: A master regulator of sterol and fatty acid synthesis. *J. Lipid Res.* 57:333–335. https://doi.org/10.1194/jlr.C066712
Martinon, F., X. Chen, A.-H. Lee, and L.H. Glimcher. 2010. TLR activation of the transcription factor XBP1 regulates innate immune responses in macrophages. *Nat. Immunol.* 11:411–418. https://doi.org/10.1038/ni.1857
Mennillo, E., Y.J. Kim, G. Lee, I. Rusu, R.K. Patel, L.C. Dorman, E. Flynn, S. Li, J.L. Bain, C. Andersen, et al. 2024. Single-cell and spatial multi-omics highlight effects of anti-integrin therapy across cellular compartments in ulcerative colitis. *Nat. Commun.* 15:1493. https://doi.org/10.1038/s41467-024-45665-6
Mielke, L.A., S.A. Jones, M. Raverdeau, R. Higgs, A. Stefanska, J.R. Groom, A. Misiak, L.S. Dungan, C.E. Sutton, G. Streubel, et al. 2013. Retinoic acid expression associates with enhanced IL-22 production by γδ T cells and innate lymphoid cells and attenuation of intestinal inflammation. *J. Exp. Med.* 210:1117–1124. https://doi.org/10.1084/jem.20121588
Molofsky, A.B., Van Gool F., H.-E. Liang, S.J. Van Dyken, J.C. Nussbaum, J. Lee, J.A. Bluestone, and R.M. Locksley. 2015. Interleukin-33 and interferon-γ counter-regulate group 2 innate lymphoid cell activation during immune perturbation. *Immunity*. 43:161–174. https://doi.org/10.1016/j.immuni.2015.05.019
Moro, K., H. Kabata, M. Tanabe, S. Koga, N. Takeno, M. Mochizuki, K. Fukunaga, K. Asano, T. Betsuyaku, and S. Koyasu. 2016. Interferon and IL-27 antagonize the function of group 2 innate lymphoid cells and type 2 innate immune responses. *Nat. Immunol.* 17:76–86. https://doi.org/10.1038/ni.3309
Moschen, A.R., H. Tilg, and T. Raine. 2019. IL-12, IL-23 and IL-17 in IBD: Immunobiology and therapeutic targeting. *Nat. Rev. Gastroenterol. Hepatol.* 16:185–196. https://doi.org/10.1038/s41575-018-0084-8
Nagashima, H., T. Mahlakõiv, H.-Y. Shih, F.P. Davis, F. Meylan, Y. Huang, O.J. Harrison, C. Yao, Y. Mikami, J.F. Urban Jr., et al. 2019. Neuropeptide CGRP limits group 2 innate lymphoid cell responses and constrains type 2 inflammation. *Immunity*. 51:682–695.e6. https://doi.org/10.1016/j.immuni.2019.06.009
Nalleweg, N., M.T. Chiriac, E. Podstawa, C. Lehmann, T.T. Rau, R. Atreya, E. Krauss, G. Hundorfean, S. Fichtner-Feigl, A. Hartmann, et al. 2015. IL-9 and its receptor are predominantly involved in the pathogenesis of UC. *Gut*. 64:743–755. https://doi.org/10.1136/gutjnl-2013-305947
Neurath, M.F. 2024. Strategies for targeting cytokines in inflammatory bowel disease. *Nat. Rev. Immunol.* 24:559–576. https://doi.org/10.1038/s41577-024-01008-6
Nishitoh, H., A. Matsuzawa, K. Tobiume, K. Saegusa, K. Takeda, K. Inoue, S. Hori, A. Kakizuka, and H. Ichijo. 2002. ASK1 is essential for endoplasmic reticulum stress-induced neuronal cell death triggered by expanded polyglutamine repeats. *Genes Dev.* 16:1345–1355. https://doi.org/10.1101/gad.992302
Nussbaum, J.C., S.J. Van Dyken, J. von Moltke, L.E. Cheng, A. Mohapatra, A.B. Molofsky, E.E. Thornton, M.F. Krummel, A. Chawla, H.-E. Liang, and R.M. Locksley. 2013. Type 2 innate lymphoid cells control eosinophil homeostasis. *Nature*. 502:245–248. https://doi.org/10.1038/nature12526
Oikawa, D., M. Tokuda, A. Hosoda, and T. Iwawaki. 2010. Identification of a consensus element recognized and cleaved by IRE1 alpha. *Nucleic Acids Res.* 38:6265–6273. https://doi.org/10.1093/nar/gkq452
Pan, Y., Y. Liu, H. Guo, M.S. Jabir, X. Liu, W. Cui, and D. Li. 2017. Associations between folate and vitamin B12 levels and inflammatory bowel disease: A meta-analysis. *Nutrients*. 9:382. https://doi.org/10.3390/nu9040382
Qiu, J., J.J. Heller, X. Guo, Z.-m.E. Chen, K. Fish, Y.-X. Fu, and L. Zhou. 2012. The aryl hydrocarbon receptor regulates gut immunity through modulation of innate lymphoid cells. *Immunity*. 36:92–104. https://doi.org/10.1016/j.immuni.2011.11.011
Rao, J., S. Yue, Y. Fu, J. Zhu, X. Wang, R.W. Busuttil, J.W. Kupiec-Weglinski, L. Lu, and Y. Zhai. 2014. ATF6 mediates a pro-inflammatory synergy between ER stress and TLR activation in the pathogenesis of liver ischemia-reperfusion injury. *Am. J. Transpl.* 14:1552–1561. https://doi.org/10.1111/ajt.12711
Rao, Z., S. Liu, Z. Li, Q. Wang, F. Gao, H. Peng, D. Ren, Y. Zang, H. Li, Y. Li, et al. 2024. Alarmin-loaded extracellular lipid droplets induce airway neutrophil infiltration during type 2 inflammation. *Immunity*. 57: 2514–2529.e7. https://doi.org/10.1016/j.immuni.2024.09.001
Ren, X., X. Wang, G. Zheng, S. Wang, Q. Wang, M. Yuan, T. Xu, J. Xu, P. Huang, and M. Ge. 2024. Targeting one-carbon metabolism for cancer immunotherapy. *Clin. Transl. Med.* 14:e1521. https://doi.org/10.1002/ctm2.1521
Ri, M., E. Tashiro, D. Oikawa, S. Shinjo, M. Tokuda, Y. Yokouchi, T. Narita, A. Masaki, A. Ito, J. Ding, et al. 2012. Identification of Toyocamycin, an agent cytotoxic for multiple myeloma cells, as a potent inhibitor of ER stress-induced XBP1 mRNA splicing. *Blood Cancer J.* 2:e79. https://doi.org/10.1038/bcj.2012.26
Schneider-Poetsch, T., J. Ju, D.E. Eyler, Y. Dang, S. Bhat, W.C. Merrick, R. Green, B. Shen, and J.O. Liu. 2010. Inhibition of eukaryotic translation elongation by cycloheximide and lactimidomycin. *Nat. Chem. Biol.* 6: 209–217. https://doi.org/10.1038/nchembio.304
Sha, H., Y. He, H. Chen, C. Wang, A. Zenno, H. Shi, X. Yang, X. Zhang, and L. Qi. 2009. The IRE1alpha-XBP1 pathway of the unfolded protein response

is required for adipogenesis. *Cell Metab.* 9:556–564. https://doi.org/10.1016/j.cmet.2009.04.009

Sharma, T.T., R.R. Rabizadeh, V.S. Prabhakar, M.I. Bury, and A.K. Sharma. 2022. Evolving experimental platforms to evaluate ulcerative colitis. *Adv. Biol. (Weinh).* 6:e2200018. https://doi.org/10.1002/adbi.202200018

Shinkai, Y., G. Rathbun, K.P. Lam, E.M. Oltz, V. Stewart, M. Mendelsohn, J. Charron, M. Datta, F. Young, A.M. Stall, and F.W. Alt. 1992. RAG-2-DEFICIENT mice lack mature lymphocytes owing to inability to initiate V(D)J rearrangement. *Cell.* 68:855–867. https://doi.org/10.1016/0092-8674(92)90029-c

Shohan, M., M. Sabzevary-Ghahfarokhi, N. Bagheri, H. Shirzad, G. Rahimian, A. Soltani, M. Ghatreh-Samani, F. Deris, K. Tahmasbi, E. Shahverdi, and F. Fathollahi. 2018. Intensified Th9 response is associated with the immunopathogenesis of active ulcerative colitis. *Immunol. Invest.* 47:700–711. https://doi.org/10.1080/08820139.2018.1486411

Siegel, M.R., and H.D. Sisler. 1963. Inhibition of protein synthesis in vitro by cycloheximide. *Nature.* 200:675–676. https://doi.org/10.1038/200675a0

Solomon, D.H., R.J. Glynn, E.W. Karlson, F. Lu, C. Corrigan, J. Colls, C. Xu, J. MacFadyen, M. Barbhaiya, N. Berliner, et al. 2020. Adverse effects of low-dose methotrexate A randomized trial. *Ann. Intern. Med.* 172:369–380. https://doi.org/10.7326/m19-3369

Song, M., T.A. Sandoval, C.-S. Chae, S. Chopra, C. Tan, M.R. Rutkowski, M. Raundhal, R.A. Chaurio, K.K. Payne, C. Konrad, et al. 2018. IRE1α-XBP1 controls T cell function in ovarian cancer by regulating mitochondrial activity. *Nature.* 562:423–428. https://doi.org/10.1038/s41586-018-0597-x

Spolski, R., P. Li, and W.J. Leonard. 2018. Biology and regulation of IL-2: From molecular mechanisms to human therapy. *Nat. Rev. Immunol.* 18:648–659. https://doi.org/10.1038/s41577-018-0046-y

Stillie, R., and A.W. Stadnyk. 2009. Role of TNF receptors, TNFR1 and TNFR2, in dextran sodium sulfate-induced colitis. *Inflamm. Bowel Dis.* 15:1515–1525. https://doi.org/10.1002/ibd.20951

Turner, J.-E., P.J. Morrison, C. Wilhelm, M. Wilson, H. Ahlfors, J.-C. Renauld, U. Panzer, H. Helmby, and B. Stockinger. 2013. IL-9-mediated survival of type 2 innate lymphoid cells promotes damage control in helminth-induced lung inflammation. *J. Exp. Med.* 210:2951–2965. https://doi.org/10.1084/jem.20130071

Upton, J.-P., L. Wang, D. Han, E.S. Wang, N.E. Huskey, L. Lim, M. Truitt, M.T. McManus, D. Ruggero, A. Goga, et al. 2012. IRE1α cleaves select microRNAs during ER stress to derepress translation of proapoptotic caspase-2. *Science.* 338:818–822. https://doi.org/10.1126/science.1226191

Urano, F., Wang X., A. Bertolotti, Zhang Y., P. Chung, H.P. Harding, and D. Ron. 2000. Coupling of stress in the ER to activation of JNK protein kinases by transmembrane protein kinase IRE1. *Science.* 287:664–666. https://doi.org/10.1126/science.287.5453.664

Vivier, E., D. Artis, M. Colonna, A. Diefenbach, J.P. Di Santo, Eberl G., S. Koyasu, R.M. Locksley, A.N.J. McKenzie, R.E. Mebius, et al. 2018. Innate lymphoid cells: 10 Years on. *Cell.* 174:1054–1066. https://doi.org/10.1016/j.cell.2018.07.017

von Moltke, J., M. Ji, H.-E. Liang, and R.M. Locksley. 2016. Tuft-cell-derived IL-25 regulates an intestinal ILC2-epithelial response circuit. *Nature.* 529:221–225. https://doi.org/10.1038/nature16161

Wallrapp, A., P.R. Burkett, S.J. Riesenfeld, S.-J. Kim, E. Christian, R.-E.E. Abdulnour, P.I. Thakore, A. Schnell, C. Lambden, R.H. Herbst, et al. 2019. Calcitonin gene-related peptide negatively regulates alarmin-driven type 2 innate lymphoid cell responses. *Immunity.* 51:709–723.e6. https://doi.org/10.1016/j.immuni.2019.09.005

Walter, P., and D. Ron. 2011. The unfolded protein response: From stress pathway to homeostatic regulation. *Science.* 334:1081–1086. https://doi.org/10.1126/science.1209038

Wang, Q., H. Zhou, Q. Bu, S. Wei, L. Li, J. Zhou, S. Zhou, W. Su, M. Liu, Z. Liu, et al. 2022. Role of XBP1 in regulating the progression of non-alcoholic steatohepatitis. *J. Hepatol.* 77:312–325. https://doi.org/10.1016/j.jhep.2022.02.031

Wang, X., J. Cai, B. Lin, M. Ma, Y. Tao, Y. Zhou, B. Li, W. Jiang, and R. Zhou. 2021. GPR34-mediated sensing of lysophosphatidylserine released by apoptotic neutrophils activates type 3 innate lymphoid cells to mediate tissue repair. *Immunity.* 54:1123–1136.e8. https://doi.org/10.1016/j.immuni.2021.05.007

Wei, J., B.T. Harada, D. Lu, R. Ma, B. Gao, Y. Xu, E. Montauti, N. Mani, S.M. Chaudhuri, S. Gregory, et al. 2021. HRD1-mediated METTL14 degradation regulates m6A mRNA modification to suppress ER proteotoxic liver disease. *Mol. Cell.* 81:5052–5065.e6. https://doi.org/10.1016/j.molcel.2021.10.028

Wilhelm, C., K. Hirota, B. Stieglitz, J. Van Snick, M. Tolaini, K. Lahl, T. Sparwasser, H. Helmby, and B. Stockinger. 2011. An IL-9 fate reporter demonstrates the induction of an innate IL-9 response in lung inflammation. *Nat. Immunol.* 12:1071–1077. https://doi.org/10.1038/ni.2133

Xu, F., and L. Wang. 2024. Deciphering ER stress-unfolded protein response relationship by visualizing unfolded proteins in the ER. *Cell Rep.* 43:114358. https://doi.org/10.1016/j.celrep.2024.114358

Xu, H., J. Ding, C.B.M. Porter, A. Wallrapp, M. Tabaka, S. Ma, S. Fu, X. Guo, S.J. Riesenfeld, C. Su, et al. 2019. Transcriptional atlas of intestinal immune cells reveals that neuropeptide α-CGRP modulates group 2 innate lymphoid cell responses. *Immunity.* 51:696–708.e9. https://doi.org/10.1016/j.immuni.2019.09.004

Yang, Z., Y. Huo, S. Zhou, J. Guo, X. Ma, T. Li, C. Fan, and L. Wang. 2022. Cancer cell-intrinsic XBP1 drives immunosuppressive reprogramming of intratumoral myeloid cells by promoting cholesterol production. *Cell Metab.* 34:2018–2035.e8. https://doi.org/10.1016/j.cmet.2022.10.010

Yin, Z., Y. Zhou, Turnquist H.R., and Q. Liu. 2022. Neuro-epithelial-ILC2 crosstalk in barrier tissues. *Trends Immunol.* 43:901–916. https://doi.org/10.1016/j.it.2022.09.006

Zaiss, D.M.W., W.C. Gause, L.C. Osborne, and D. Artis. 2015. Emerging functions of amphiregulin in orchestrating immunity, inflammation, and tissue repair. *Immunity.* 42:216–226. https://doi.org/10.1016/j.immuni.2015.01.020

Zeng, X., X. Xiao, S. Hu, W. He, G. Wu, X. Geng, J. Fan, L. Ma, J. Liu, Z. Liu, and P. Yang. 2022. XBP1 is required in Th2 polarization induction in airway allergy. *Theranostics.* 12:5337–5349. https://doi.org/10.7150/thno.75100

Zheng, M., Y. Zhai, Y. Yu, J. Shen, S. Chu, E. Focaccia, W. Tian, S. Wang, X. Liu, X. Yuan, et al. 2024. TNF compromises intestinal bile-acid tolerance dictating colitis progression and limited infliximab response. *Cell Metab.* 36:2086–2103.e9. https://doi.org/10.1016/j.cmet.2024.06.008

Zhou, C.-M., L.-M. Luo, P. Lin, Q. Pu, B. Wang, S. Qin, Q. Wu, X.-J. Yu, and M. Wu. 2021. Annexin A2 regulates unfolded protein response via IRE1-XBP1 axis in macrophages during P. aeruginosa infection. *J. Leukoc. Biol.* 110:375–384. https://doi.org/10.1002/jlb.3a1219-686rr

Zhou, L., W. Zhou, A.M. Joseph, C. Chu, G.G. Putzel, B. Fang, F. Teng, M. Lyu, H. Yano, K.I. Andreasson, et al. 2022. Group 3 innate lymphoid cells produce the growth factor HB-EGF to protect the intestine from TNF-mediated inflammation. *Nat. Immunol.* 23:251–261. https://doi.org/10.1038/s41590-021-01110-0

Zhou, Y., W. Wang, C. Zhao, Y. Wang, H. Wu, X. Sun, Y. Guan, and Y. Zhang. 2018. Prostaglandin E2 inhibits group 2 innate lymphoid cell activation and allergic airway inflammation through E-prostanoid 4-cyclic adenosine monophosphate signaling. *Front. Immunol.* 9:501. https://doi.org/10.3389/fimmu.2018.00501

Zhu, X.-M., F.-H. Yao, Y.-M. Yao, N. Dong, Y. Yu, and Z.-y. Sheng. 2012. Endoplasmic reticulum stress and its regulator XBP-1 contributes to dendritic cell maturation and activation induced by high mobility group box-1 protein. *Int. J. Biochem. Cell Biol.* 44:1097–1105. https://doi.org/10.1016/j.biocel.2012.03.018

JEM

Supplemental material

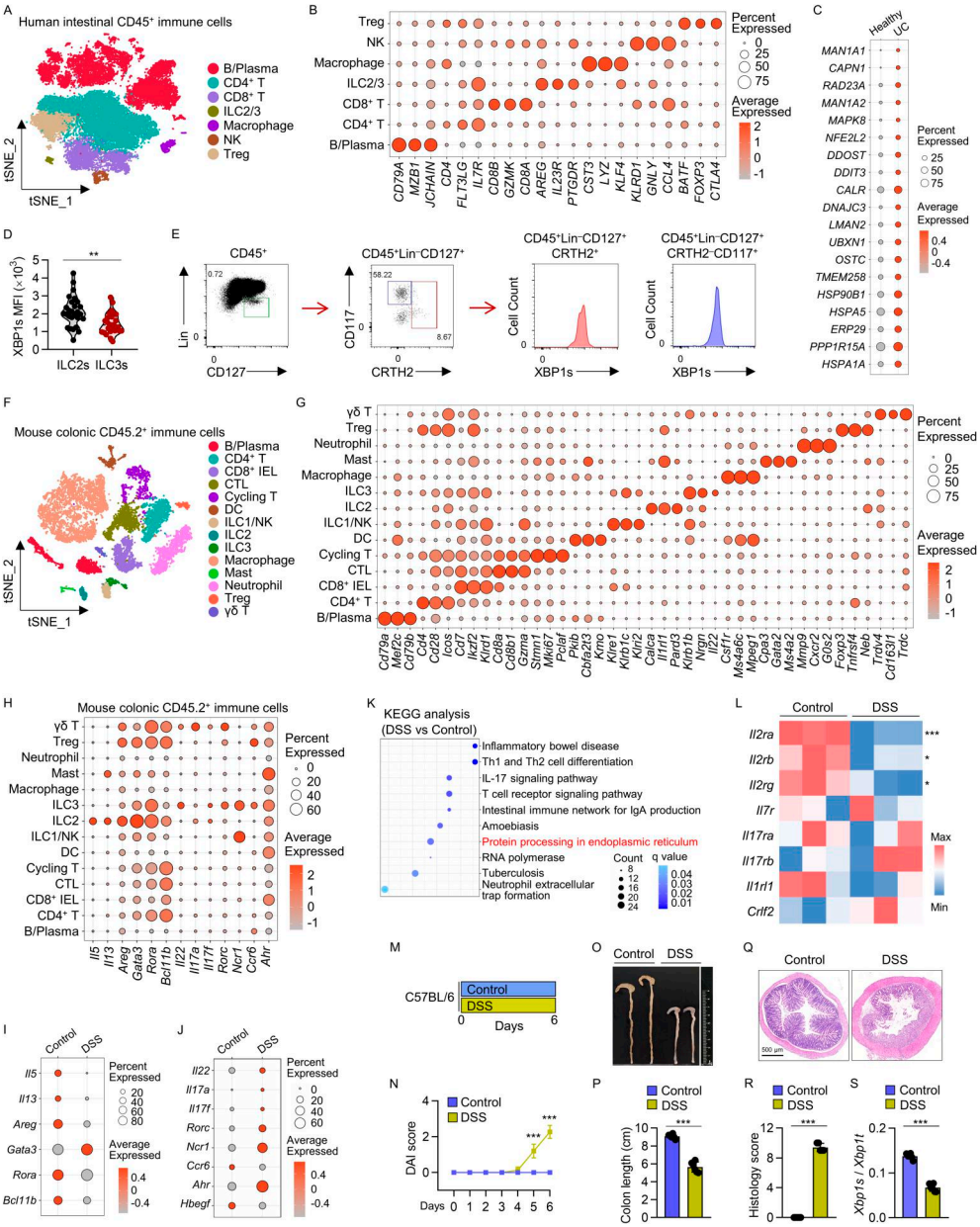

Figure S1. **Impaired function and changed protein processing pathway in ER in colonic ILC2s during colitis. (A)** Purified CD45⁺ immune cells from the intestinal biopsies of patients with UC or healthy donors were analyzed by scRNA-seq. The tSNE visualizations of CD45⁺ immune cells, with the included subsets annotated. Data are from GSE125527. **(B)** Dot plot showed the expression of cell-defining signature genes across all cell types of human intestinal CD45⁺ immune cells. **(C)** Dot plot showed the upregulation of genes involved in the protein processing in ER pathways in ILC2/3 cells of patients with UC in Fig. 1 C. **(D)** Flow cytometry analysis of the MFI of XBP1s in colonic ILC2s (CD45⁺Lin⁻CD127⁺CRTH2⁺) and ILC3s (CD45⁺Lin⁻CD127⁺CRTH2⁻CD117⁺) of healthy donors (n = 27). **(E)** Schematic of gating strategy used to identify human colonic ILCs. Gating methods for ILC2 (CD45⁺Lin⁻CD127⁺CRTH2⁺), and ILC3 (CD45⁺Lin⁻CD127⁺CRTH2⁻CD117⁺) subsets are shown. **(F)** Mid-colon tissues were harvested from mice treated with 3% DSS for 6 days and subjected to scRNA-seq analysis. The scRNA-seq data served as the control group were generated from untreated mice by our team (GSE210415). tSNE visualizations of all cell types of mouse colonic CD45⁺ immune cells. 14 clusters characterized by lineage-specific and cluster-enriched genes were identified by integrated analysis. Colors represent the annotated cell subtypes. **(G)** Dot plot showed the abundance and intensity of lineage-specific marker gene expression across all cell types of mouse colonic CD45⁺ immune cells. **(H)** Dot plot showed the abundance and intensity of the signature genes of ILC2s or ILC3s in all cell types of mouse colonic CD45⁺ immune cells. **(I and J)** Dot plot showed the levels of representative ILC2 feature genes in ILC2s (I) and ILC3 signature genes in ILC3s (J) from DSS-treated or control mice. **(K)** ILC2s identified in Fig. 1 K were extracted for KEGG pathway enrichment analysis. **(L)** Heatmap of the cytokine receptors responsible for ILC2 survival or activation by conducting SMART-seq analysis with sorted colonic ILC2s of mice treated with 3% DSS for 6 days or control mice. **(M–R)** WT mice were fed with 3% DSS for 6 days to induce colitis model. Experimental design (M). DAI scores (N) were monitored at the indicated time points. Representative large intestine images (O). Lengths of colons (P). Representative H&E staining of the colon. Scale bar, 500 μm (Q). Histological severity scores of colons (R). Data were compiled from two independent experiments and are shown as the mean ± SD (n = 5 per group). **(S)** Large intestinal ILC2s (Lin⁻CD127⁺KLRG1⁺) were sorted from the mice treated with 3% DSS for 6 days and control mice, followed by qRT-PCR analysis. The bar graph showed the *Xbp1* mRNA splicing in ILC2s. Data were compiled from two independent experiments. Data are shown as the mean ± SD (n = 6 per group). *P < 0.05, ***P < 0.001. tSNE, t-distributed stochastic neighbor embedding.

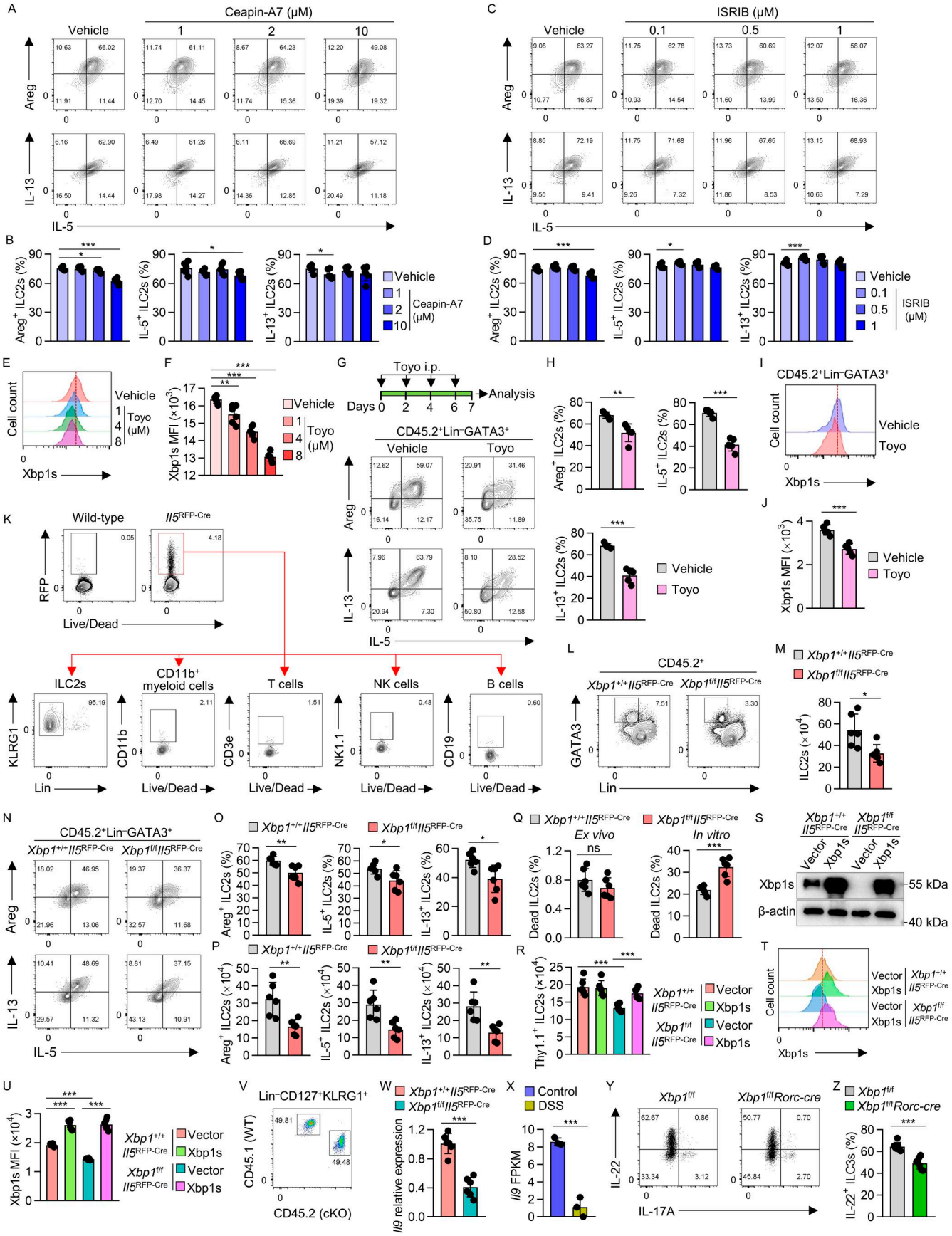

Figure S2. **Xbp1s regulates gut ILC2s in a cell-intrinsic manner. (A–D)** Sorted large intestinal ILC2s ($Lin^-CD127^+KLRG1^+$) were cultured for 5 days in the presence of IL-2, IL-7, IL-25, and IL-33 (10 ng/ml each), followed by treatment with Ceapin-A7 and ISRIB, respectively, at the indicated concentrations for 16 h. Flow cytometry analyses of Areg, IL-5, and IL-13 expression (Ceapin-A7, A; ISRIB, C) after gating on $CD45.2^+Lin^-GATA3^+$ ILC2s. Percentages of $Areg^+$, $IL\text{-}5^+$, and $IL\text{-}13^+$ ILC2s (Ceapin-A7, B; ISRIB, D). Data were compiled from two independent experiments. Data are shown as the mean ± SD (n = 6 per group). **(E and F)** Flow cytometry analysis of Xbp1s expression in ILC2s ($CD45.2^+Lin^-GATA3^+$) (E) following treatment with Toyo at indicated concentrations. MFI of Xbp1s in ILC2s (F). Data were compiled from two independent experiments. Data are shown as the mean ± SD (n = 6 per group). **(G–J)** WT mice were injected i.p. with Toyo (0.7 mg/kg) every other day for four doses, followed by large intestine harvesting to analyze ILC2 function. Experimental design (G, top). Flow cytometry analysis of Areg, IL-5, and IL-13 expression in ILC2s ($CD45.2^+Lin^-GATA3^+$) from the large intestine LPLs (G, bottom). Percentages of $Areg^+$, $IL\text{-}5^+$, and $IL\text{-}13^+$ ILC2s (H). Flow cytometry analysis of Xbp1s expression in ILC2s (I). MFI of Xbp1s in ILC2s (J). Data were compiled from two independent experiments. Data are shown as the mean ± SD (n = 5 per group). **(K)** Representative flow cytometry plots show frequencies of RFP^+ ($IL\text{-}5^+$) cells on the following colonic various immune cell subsets: ILC2s (Lin^-KLRG1^+), B cells ($CD19^+$), $CD11b^+$ myeloid cells ($CD11b^+$), $CD3e^+$ T cells ($CD3e^+$), NK cells ($NK1.1^+$). **(L–P)** Large intestine was harvested from *Xbp1*$^{f/f}$*Il5*$^{RFP\text{-}Cre}$ and *Xbp1*$^{+/+}$*Il5*$^{RFP\text{-}Cre}$ mice for subsequent analysis. Flow cytometry analysis of GATA3 expression after gating on $CD45.2^+Lin^-$ cells in large intestinal LPLs (L). Absolute numbers of ILC2s ($CD45.2^+Lin^-GATA3^+$) (M). Flow cytometry analysis of Areg, IL-5, and IL-13 expression in ILC2s (N). Percentages (O) and absolute numbers (P) of $Areg^+$, $IL\text{-}5^+$, and $IL\text{-}13^+$ ILC2s. Data were compiled from two independent experiments. Data are shown as the mean ± SD (n = 5 per group). **(Q)** Large intestines were harvested from *Xbp1*$^{+/+}$*Il5*$^{RFP\text{-}Cre}$ or *Xbp1*$^{f/f}$*Il5*$^{RFP\text{-}Cre}$ mice for analysis of ILC2 cell death at steady state. Flow cytometry analysis of $Aqua^+$Annexin V^+ proportion after gating on $CD45.2^+Lin^-CD127^+KLRG1^+$ ILC2s in LPLs, and the percentages of dead ILC2s (left). Sorted large intestinal ILC2s ($Lin^-CD127^+KLRG1^+$) from *Xbp1*$^{+/+}$*Il5*$^{RFP\text{-}Cre}$ and *Xbp1*$^{f/f}$*Il5*$^{RFP\text{-}Cre}$ mice were cultured in the presence of IL-2, IL-7, IL-25 (10 ng/ml each) for 9 days and then detected cell death. Flow cytometry analysis of Aqua and Annexin V expression in expanded ILC2s, and the percentages of dead ILC2s (right). Data were compiled from two independent experiments and are shown as the mean ± SD (n = 6 per group). **(R–U)** Large intestinal ILC2s ($Lin^-CD127^+KLRG1^+$) were sorted from *Xbp1*$^{f/f}$*Il5*$^{RFP\text{-}Cre}$ or littermate *Xbp1*$^{+/+}$*Il5*$^{RFP\text{-}Cre}$ mice and underwent retroviral transduction of Xbp1s with IRES-controlled Thy1.1 expression to label transduced cells. $Thy1.1^+$ cells after gating on $Lin^-CD45.2^+$ were sorted and cultured for 4 days. Numbers of $Thy1.1^+$ ILC2s in the indicated group (R). The protein levels of Xbp1s in the indicated group were detected by western blotting. β-Actin served as the internal control (S). Analysis of Xbp1s expression in ILC2s by flow cytometry (T). MFI of Xbp1s in ILC2s (U). Data were compiled from two independent experiments. Data are shown as the mean ± SD (n = 6 per group). **(V)** Sorted large intestinal ILC2s ($Lin^-CD127^+KLRG1^+$) from WT (*Xbp1*$^{+/+}$*Il5*$^{RFP\text{-}Cre}$) (CD45.1/CD45.1) or cKO (*Xbp1*$^{f/f}$*Il5*$^{RFP\text{-}Cre}$) (CD45.2/CD45.2) mice were mixed equally and transferred into *Rag2*$^{-/-}$*Il2rg*$^{-/-}$ mice. Flow cytometry analyses of CD45.1 and CD45.2 expression ratio of mixed ILC2s. **(W)** *Il9* expression in sorted large intestinal ILC2s ($Lin^-CD127^+KLRG1^+$) from *Xbp1*$^{+/+}$*Il5*$^{RFP\text{-}Cre}$ or *Xbp1*$^{f/f}$*Il5*$^{RFP\text{-}Cre}$ mice was assessed by qRT-PCR. Data were compiled from two independent experiments and are shown as the mean ± SD (n = 6 per group). **(X)** SMART-seq was performed on sorted large intestinal ILC2s from 3% DSS-treated (6 days) mice or control mice. The FPKM of *Il9* was analyzed based on SMART-seq data. **(Y and Z)** *Xbp1*$^{f/f}$ and *Xbp1*$^{f/f}$*Rorc-cre* mice were fed with 3% DSS for 6 days to induce colitis. Flow cytometry analysis of IL-22 expression after gating on $CD45.2^+Lin^-ROR\gamma t^+$ ILC3s in the large intestinal LPLs (Y). Percentages of $IL\text{-}22^+$ ILC3s (Z). Data were compiled from two independent experiments and are shown as the mean ± SD (n = 7 per group). *P < 0.05, **P < 0.01, ***P < 0.001. Source data are available for this figure: SourceData FS2.

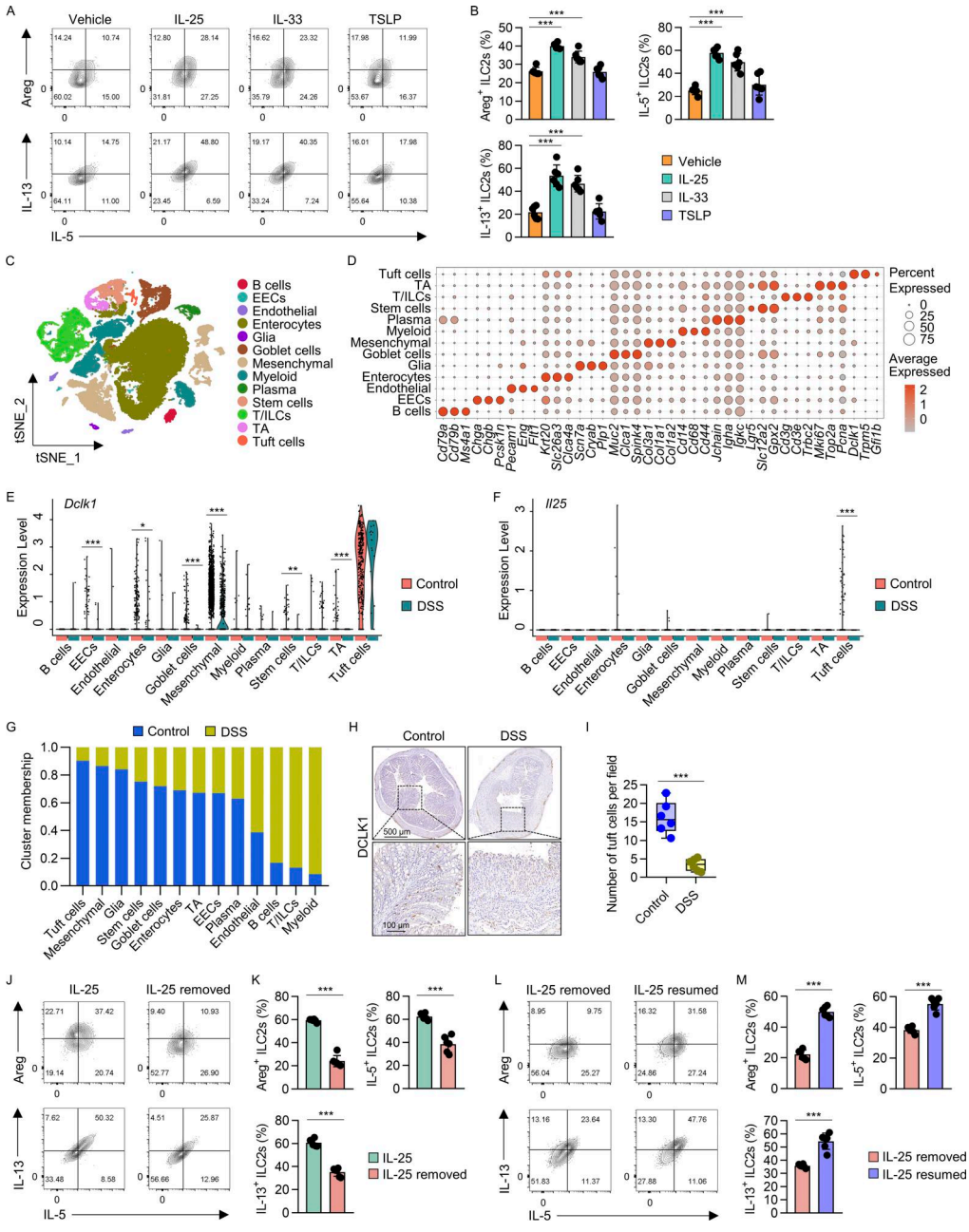

Figure S3. **IL-25 sustains gut ILC2 function, and the production of IL-25 in tuft cells decreased during colitis. (A and B)** Sorted large intestinal ILC2s (Lin⁻CD127⁺KLRG1⁺) were cultured in complete IMDM containing IL-2 (10 ng/ml) and IL-7 (10 ng/ml), and treated for 16 h in the presence of IL-25 (10 ng/ml), IL-33 (10 ng/ml), or TSLP (10 ng/ml). Flow cytometry analyses of Areg, IL-5, and IL-13 expression after gating on CD45.2⁺Lin⁻GATA3⁺ ILC2s (A). Percentages of Areg⁺, IL-5⁺, and IL-13⁺ ILC2s (B). Data were compiled from two independent experiments. Data are shown as the mean ± SD (n = 6 per group). **(C–G)** Mid-colon tissues were harvested from mice treated with 3% DSS for 6 days and subjected to scRNA-seq analysis. The scRNA-seq data served as the control group were generated from untreated mice by our team (GSE210415). (C) tSNE visualizations of all cell types of colonic cells of mice. 13 clusters characterized by lineage-specific and cluster-enriched gene were identified by integrated analysis. Colors represent the corresponding annotated cell subtypes. (D) Dot plot showed the abundance and intensity of lineage-specific marker gene expression across all cell types of colonic cells in mice. *Dclk1* (E) and *Il25* (F) levels in all cell types of intestinal tissues of DSS-treated and control mice. **(G)** Proportions of indicated cell type among colonic tissues of DSS-treated or control mice. **(H and I)** Representative sections of mid-colon tissues from DSS-treated mice or control mice stained with DCLK1 by immunohistochemistry to visualize tuft cells. Top: scale bar, 500 µm; bottom: scale bar, 100 µm (H). Statistics graph showed the average number of DCLK1-positive tuft cells per field (I). Data are shown as the mean ± SD (n = 6 per group). **(J and K)** Sorted large intestinal ILC2s (Lin⁻CD127⁺KLRG1⁺) were cultured in complete IMDM containing IL-2, IL-7, and IL-25 (10 ng/ml each) for 5 days. Subsequently, the IL-25 was removed for 2 days. Flow cytometry analyses of Areg, IL-5, and IL-13 expression after gating on CD45.2⁺Lin⁻GATA3⁺ ILC2s (J). Percentages of Areg⁺, IL-5⁺, and IL-13⁺ ILC2s (K). Data were compiled from two independent experiments. Data are shown as the mean ± SD (n = 6 per group). **(L and M)** Sorted large intestinal ILC2s (Lin⁻CD127⁺KLRG1⁺) were cultured in complete IMDM containing IL-2, IL-7, and IL-25 (10 ng/ml each) for 5 days, and IL-25 was removed for 2 days, followed by restimulation with or without IL-25 (10 ng/ml) for 1 day. Analysis of Areg, IL-5, and IL-13 expression in ILC2s (CD45.2⁺Lin⁻GATA3⁺) by flow cytometry (L). Percentages of Areg⁺, IL-5⁺, and IL-13⁺ ILC2s (M). Data were compiled from two independent experiments. Data are shown as the mean ± SD (n = 6 per group). *P < 0.05, **P < 0.01, ***P < 0.001.

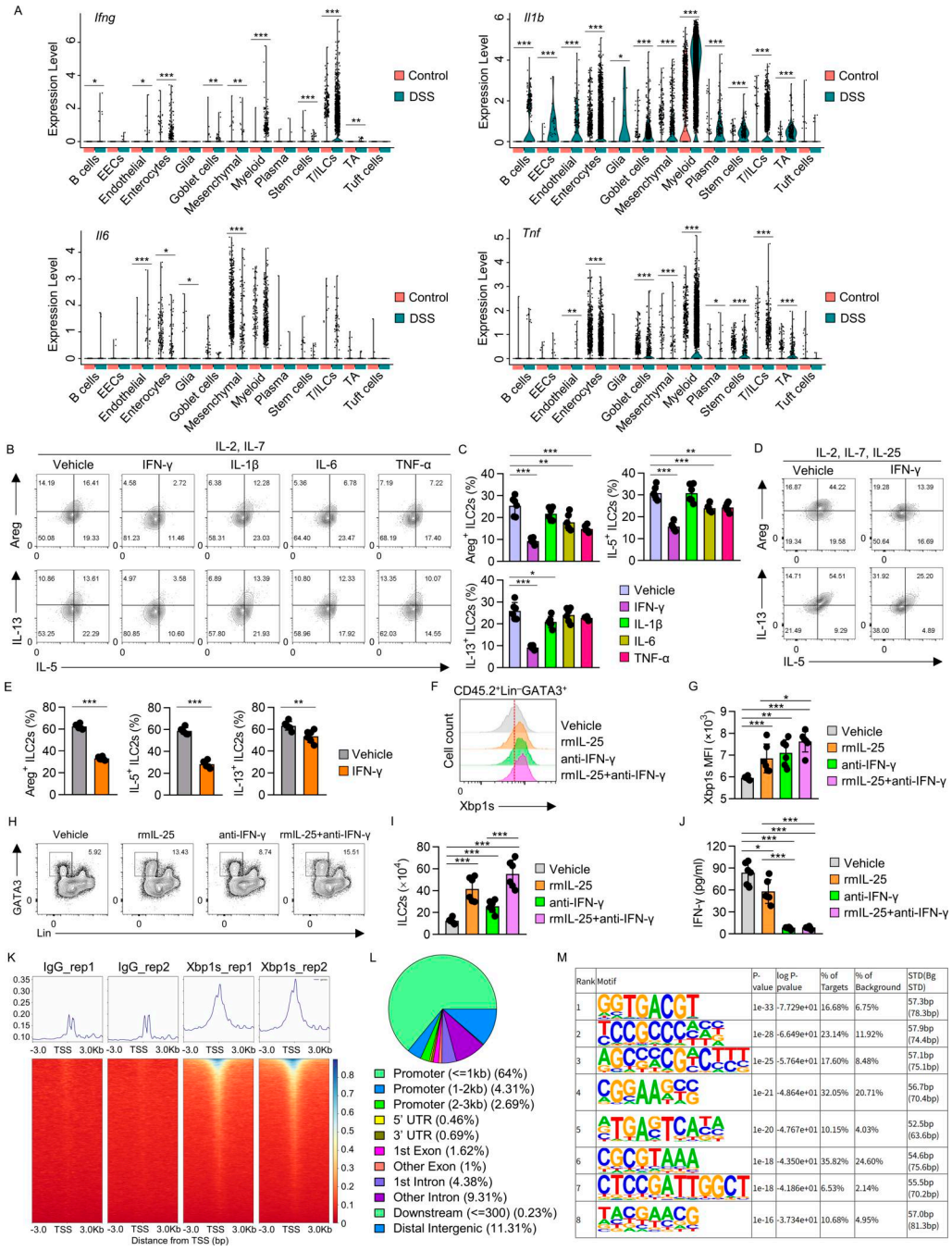

Figure S4. **Pro-inflammatory cytokine IFN-γ evidently restrains intestinal ILC2 function and CUT&Tag-seq. (A)** mRNA levels of pro-inflammatory genes, *Ifng*, *Il1b*, *Il6*, and *Tnf*, in all cell types of colonic tissues from DSS-treated and control mice were analyzed by scRNA-seq. **(B and C)** Sorted large intestinal ILC2s (Lin⁻CD127⁺KLRG1⁺) were cultured in complete IMDM containing IL-2 (10 ng/ml) and IL-7 (10 ng/ml), and co-incubated for 3 days with IFN-γ (50 ng/ml), IL-1β (50 ng/ml), IL-6 (50 ng/ml), or TNF-α (50 ng/ml), respectively. Flow cytometry analyses of Areg, IL-5, and IL-13 expression after gating on CD45.2⁻⁺Lin⁻GATA3⁺ ILC2s (B). Percentages of Areg⁺, IL-5⁺, and IL-13⁺ ILC2s (C). Data were compiled from two independent experiments. Data are shown as the mean ± SD (n = 6 per group). **(D and E)** Sorted large intestinal ILC2s (Lin⁻CD127⁺KLRG1⁺) were stimulated with the IFN-γ (500 ng/ml) for 3 days in complete IMDM containing IL-2, IL-7, and IL-25 (10 ng/ml each). Flow cytometry analyses of Areg, IL-5, and IL-13 expression after gating on CD45.2⁺Lin⁻GATA3⁺ ILC2s (D). Percentages of Areg⁺, IL-5⁺, and IL-13⁺ ILC2s (E). Data were compiled from two independent experiments. Data are shown as the mean ± SD (n = 6 per group). **(F–J)** WT mice were administered 3% DSS in drinking water for 6 days to induce colitis, rmIL-25 (0.4 μg) was injected i.p. five doses daily from the onset of colitis induction, while anti-IFN-γ (1 mg) was injected i.p. on days −1, 2, and 5; the mice were sacrificed for analysis on day 6. Analysis of Xbp1s expression in ILC2s (CD45.2⁺Lin⁻GATA3⁺) from large intestinal LPLs by flow cytometry (F). MFI of Xbp1s in ILC2s (G). Flow cytometry analysis of GATA3 expression after gating on CD45.2⁺Lin⁻ cells in large intestinal LPLs (H). Absolute numbers of ILC2s (CD45.2⁺Lin⁻GATA3⁺) (I). Serum IFN-γ concentrations were detected by ELISA kit (J). Data were compiled from two independent experiments. Data are shown as the mean ± SD (n = 6 per group). **(K)** Density plots (top) and heatmaps (bottom) of Xbp1s binding to the TSS regions (from −3 to 3 kb) in mouse colonic ILC2s. **(L)** Gene component analysis showed percent distribution of Xbp1s binding sites measured by CUT&Tag-seq, including promoter, 5′UTR, 3′UTR, exon, intron, and intergenic regions. **(M)** Binding motif analysis of Xbp1s based on CUT&Tag-seq peaks in ILC2s. *P < 0.05, **P < 0.01, ***P < 0.001.

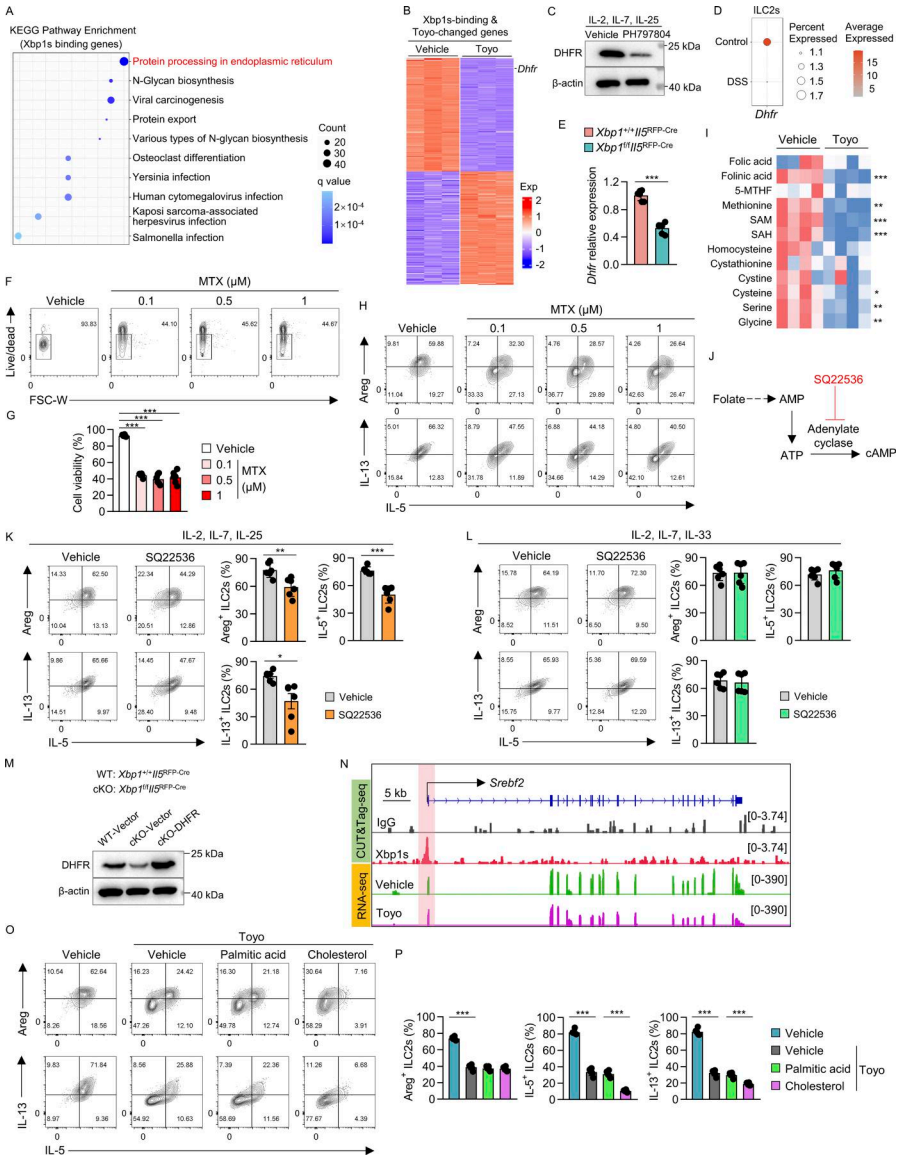

Figure S5. **Xbp1s targets DHFR to regulate folate-mediated 1C metabolism in gut ILC2s. (A)** KEGG pathway enrichment analysis of the Xbp1s binding genes (Table S5). **(B)** Heatmap of overlapping genes between Xbp1s-binding and Toyo-changed genes described in Fig. 5 A; the overlapping genes are listed in Table S6. **(C)** Sorted large intestinal ILC2s (Lin$^-$CD127$^+$KLRG1$^+$) were cultured for 5 days, followed by treatment with PH797804 at 10 μM for 16 h. The protein levels of DHFR were detected by western blotting. β-Actin served as the internal control. Data are representative of three independent experiments. **(D)** *Dhfr* expression in ILC2s was analyzed by scRNA-seq of the colon from DSS-treated and control mice. **(E)** *Dhfr* expression in sorted large intestinal ILC2s (Lin$^-$CD127$^+$KLRG1$^+$) from *Xbp1*$^{+/+}$*Il5*$^{RFP\text{-}Cre}$ or *Xbp1*$^{f/f}$*Il5*$^{RFP\text{-}Cre}$ mice was assessed by qRT-PCR. Data were compiled from two independent experiments and are shown as the mean ± SD (n = 6 per group). **(F–H)** Sorted large intestinal ILC2s (Lin$^-$CD127$^+$KLRG1$^+$) were cultured in the presence of IL-2, IL-7, and IL-25 (10 ng/ml each), with or without MTX co-incubation for 3 days at the indicated concentrations. Flow cytometry analysis of viability in ILC2s (CD45.2$^+$Lin$^-$GATA3$^+$) (F), and the corresponding statistical graphs (G). Data are representative of two independent experiments. Data are shown as the mean ± SD (n = 6 per group). Flow cytometry analyses of Areg, IL-5, and IL-13 expression in ILC2s (H). **(I)** Sorted large intestinal ILC2s (Lin$^-$CD127$^+$KLRG1$^+$) were cultured in complete IMDM containing IL-2, IL-7, and IL-25 (10 ng/ml each) for 5 days, and then treated with Toyo at 4 μM for 16 h, followed by the targeted metabolomics analysis of 1C metabolism (n = 4 per group). Heatmap of folate metabolites in indicated ILC2s. **(J)** Schematic diagram of SQ22536 inhibiting cAMP generation. **(K and L)** Sorted large intestinal ILC2s (Lin$^-$CD127$^+$KLRG1$^+$) were cultured in complete IMDM containing IL-2, IL-7, and IL-25 (K) or IL-33 (L) (10 ng/ml each), and then treated with SQ22536 at 1 mM for 48 h. Flow cytometry analyses of Areg, IL-5, and IL-13 expression after gating on CD45.2$^+$Lin$^-$GATA3$^+$ ILC2s, and percentages of Areg$^+$, IL-5$^+$, and IL-13$^+$ ILC2s. Data were compiled from two independent experiments. Data are shown as the mean ± SD (n = 6 per group). **(M)** Large intestinal ILC2s (Lin$^-$CD127$^+$KLRG1$^+$) were sorted from *Xbp1*$^{f/f}$*Il5*$^{RFP\text{-}Cre}$ or *Xbp1*$^{+/+}$*Il5*$^{RFP\text{-}Cre}$ mice and underwent retroviral transduction of DHFR with IRES-controlled Thy1.1 expression to label transduced cells. Thy1.1$^+$ cells after gating on Lin$^-$CD45.2$^+$ were sorted and cultured for 4 days. Levels of DHFR in indicated ILC2s were detected by western blotting. β-Actin served as the internal control. Data are representative of three independent experiments. **(N)** Track views of Xbp1s CUT&Tag-seq peaks in colonic ILC2s of mice, and RNA-seq in ILC2s treated with Toyo at genes *Srebf2*. **(O and P)** Sorted large intestinal ILC2s (Lin$^-$CD127$^+$KLRG1$^+$) were cultured for 5 days, followed by treatment with Toyo at 4 μM, with or without palmitic acid (50 μM) and cholesterol (30 μM) for 16 h. Flow cytometry analysis of Areg, IL-5, and IL-13 expression in ILC2s (CD45.2$^+$Lin$^-$GATA3$^+$) (O). Percentages of Areg$^+$, IL-5$^+$, and IL-13$^+$ ILC2s (P). Data were compiled from two independent experiments. Data are shown as the mean ± SD (n = 6 per group). *P < 0.05, **P < 0.01, ***P < 0.001. Source data are available for this figure: SourceData FS5.

Provided online are Table S1, Table S2, Table S3, Table S4, Table S5, Table S6, Table S7, and Table S8. Table S1 lists the marker genes defining human immune cell subsets. Table S2 lists the demographic information of UC participants and healthy donors. Table S3 lists the marker genes defining mouse colonic CD45$^+$ immune cell subsets. Table S4 lists the marker genes defining all colonic cell types in mouse. Table S5 lists the Xbp1s binding genes in large intestinal ILC2s analyzed by CUT&Tag-seq. Table S6 lists the overlapping gene analysis between Xbp1s-binding genes with differentially expressed genes in toyocamycin-treated ILC2s. Table S7 lists the sequences of primers used for qRT-PCR. Table S8 lists the antibodies used for flow cytometry, and reagents and recombinant proteins used for ILC2 treatment.